SAPIENZA
UNIVERSITÀ DI ROMA

Localization of transverse impedance sources in the SPS using HEADTAIL macroparticle simulations

Università degli Studi di Roma "La Sapienza"
Facoltà di Ingegneria
Laurea specialistica in Ingegneria Elettronica

Candidato
Nicolò Biancacci
matr:1103343

Relatore:
Prof. L.Palumbo

Correlatore:
Dr. M.Migliorati
Dr. B.Salvant (CERN)

A/A: 2009/2010

Abstract

In particle accelerators, beam coupling impedances are one of the main contributors to instability phenomena that lead to particle losses and beam quality deterioration. For this reason, the impedance of these machine should be continuously monitored and main sources of impedance should be identified.

In this thesis work we present our studies on the algorithm used to detect local sources of impedance. The main assumptions behind this algorithm are described in order to understand its limitations in reconstructing the impedance location.

The phase advance response matrix is analyzed in particular for the SPS lattice, studying the different response for 90°, 180° and 270° phase advance sections. The role of beta function is also analyzed and the reconstruction matrix is then normalized on this parameter in order to have a smoother response.

The thin lenses scheme is also implemented and new analytical formulas for phase advance beating were derived. This scheme enable us to put reconstructing lenses everywhere in the lattice, and to study their positioning in more depth.

Finally, analyzing the response to known kicks enables us to set the upper and lower limits in accurate reconstruction due to the phase advance measurement accuracy and the linear response regime limit.

Estratto

In macchine come gli acceleratori di particelle, l'impedenza d'accoppiamento rappresenta una delle principali cause di instabilità che può portare a consistenti perdite e deterioramenti nella qualità del fascio. Per questo motivo, costituisce uno dei parametri costantemente sotto controllo in un acceleratore, oggetto di valutazioni globali (intera macchina) e locali (singolo elemento).

In questa tesi presentiamo alcuni studi su un algoritmo di localizzazione di impedenza trasversa. Le principali ipotesi alla base dell'algoritmo verranno analizzate con l'obiettivo di individuare i limiti nella ricostruzione della posizione dell'impedenza.

La matrice di risposta in avanzamento di fase del lattice di SPS verrà analizzata, studiando i diversi tipi di risposta relativi alle sezioni in cui si ha un avanzamento di fase rispettivamente di 90°, 180° e 270°. Considereremo anche gli effetti della funzione di betatrone nella ricostruzione, proponendo una normalizzazione della matrice di risposta a tale parametro.

Presenteremo uno schema di localizzazione d'impedenza utilizzando lenti sottili per la ricostruzione. Utili formule analitiche sono inoltre state derivate per consentire un calcolo più rapido della matrice di risposta e una maggior flessibilità nel posizionamento delle lenti.

Verranno presentati anche gli studi di linearità di risposta del sistema, determinando così i limiti superiore e inferiore per una corretta localizzazione dell'impedenza, rispettivamente l'accuratezza nella misura dell' avanzamento di fase, e il limite nella validità di risposta lineare del sistema.

Contents

Chapter 1

Introducion

An accelerator is a complex machine able to accelerate bunches of particles up to the energy requested by scientific experiments, performed in order to study the most hidden sides of Nature.

Each bunch of particles has to be constantly monitored and made stable to guarantee the correct parameters for experiments. Infact, many studies has been done to fully describe the physics of collective effects to have a complete picture of inner mechanisms behind particle interactions within the bunch itself or with the surrounding world.

The *coupling impedance* is a quantity used to describe the interaction between particles and the electromagnetic fields excited by the bunches themselves circulating in the accelerator, and it is directly correlated with the rising of instability phenomena for certain range of bunch intensities.

In order to prevent instabilities that lead to losses of particles affecting the quality of the experiments, the impedance has to be monitored, quantified and, when needed, reduced. Currently it is possible to perform measurements of the global value of impedance in an accelerator, but it is also necessary to know the quantity of impedance associated to each element in the accelerator machine. A local impedance detection algorithm was used in the past to detect the main contributors to impedance in LEP and SPS. In this thesis we will analyze the algorithm, the assumptions behind it, and its limits in reconstructing the positions of impedance sources.

In Chapter 1, we will introduce the reader to CERN history and experiments, in order to present the context to which these studies belong to, the accelerator chain and the future upgrade plans.

In Chapter 2, the transverse instability theory is introduced. Space charge, wake fields and impedances are defined. Particular attention was given to include both dipolar and quadrupolar impedance definitions, together with the classical A.W.Chao's approach to this topic. In order to let the reader understand how an impedance can be computed, we presented the frequency domain approach for two problems: a circular geometry, representing a beam-pipe, and a rectangular geometry loaded with ferrite slsb, representing a kicker. For the second one, the electromagnetic fields were also derived.

In Chapter 3, the detection algorithm is introduced. In particular, the underlying assumptions are described in order to define the limit of validity in applying the algorithm. The distinction between global and local observables to measure

impedance in accelerators is correlated to tune shift and phase advance beating signal measurements. For this reason formulas for phase advance beating in the SPS lattice are derived and used to upgrade the detection algorithm. Codes used in our simulation, *HEADTAIL*, *MAD-X*, and *SUSSIX*, are also presented, with particular attention to the phase accuracy we can reach.

In Chapter 4, we present reconstructions from our simulations. After the main limits are defined, we describe the thin lens reconstructing scheme. Studies on the quality of the response matrix are also presented in order to focus on the main issues coming from the SPS lattice irregularity. Linear response assumptions is also analyzed, leading us to define upper and lower limits for a good reconstruction: the accuracy in the measured phase and the linear approximation limit.

Chapter 2

CERN - European Organization for Nuclear Research

2.1 What is CERN

Founded in 1954, the CERN laboratory is located at the French-Swiss border, between the Jura mountains and Geneva's lake. The acronym CERN stands for *European Organization for Nuclear Research*, institution founded in 1954, with the mandate of establishing a world-class fundamental physics research organization in Europe.

CERN provides to scientists with particle accelerators, detectors, and infrastructure in order to set up experiments needed to go deeper in our understanding of matter, particle physics and Universe.

Currently, the CERN laboratory counts 20 Member States[1], 8 "Observers"[2], and provides facilities to 580 institutes and universities involving 85 nationalities [1][2].

2.2 Key events of the history of CERN

Here is a brief summary of CERN history.

1954 After the Second World War, a commission of scientists imagined creating a European atomic physics laboratory: the 29th of September 1954, CERN is founded.

1957 600 MeV Synchrocyclotron was CERN's first accelerator, providing with experiments in both nuclear and particle physics.

1959 The Proton Synchrotron (PS) accelerated protons with a beam kinetic energy of 25 GeV becoming for a brief period, the highest energy world accelerator. From 1970s, when SPS and other accelerators were commissioned, its principle role is to supply other accelerators with beam, and the machine has become one of the world's most versatile particle juggler.

[1]Member States: Austria, Belgium, Bulgaria, the Czech Republic, Denmark, Finland, France, Germany, Greece, Hungary, Italy, the Netherlands, Norway, Poland, Portugal, the Slovak Republic, Spain, Sweden, Switzerland and the United Kingdom.

[2]Observers: European Commission, India, Israel, Japan, the Russian Federation, Turkey, UNESCO and the USA.

1968 Georges Charpak, awarded the 1992 Nobel Prize in Physics for his work on particle detectors, developed the "multi-wire proportional chamber", a gas-filled box with a large number of parallel detector wires, each connected to individual amplifiers, currently used in every detecting system.

1973 Discovery of neutral currents at the Gargamelle bubble chamber: another step in understanding fundamental particles and their interactions.

1976 The SPS is commissioned. Initially it was designed to work at 300 GeV/c, now it is injecting beam in LHC at 450 GeV/c. During its long career SPS supported also proton-antiproton colliding experiments, allowing the W, Z bosons discovery in 1983.

1983 W and Z bosons discovery. Carlo Rubbia and Simon van der Meer received the Nobel Prize thanks to this discovery, the former proposing to use SPS as proton-antiproton collider, the latter inventing the stochastic cooling technique, vital for collider's operation.

1989 LEP is commissioned. Projected to provide collisions at 100 GeV, with its 27 Km circumference, LEP provided also higher energy collisions allowing detailed study of electroweak interaction.

1990 The World Wide Web was born from a Tim Berners-Lee idea of developing a distributed information system to share knowledge and data between scientists all over the world.

1995 First observation of anti-Hydrogen at Low Energy Antiproton Ring. The Universe is made in 75% by hydrogen: understanding its behavior offered a route to understanding matter-antimatter asymmetry in the Universe.

2008 - 2010 LHC starts up. The new accelerator takes the place of LEP, and will provide collision at 14 TeV design kinetic energy. After a first unlucky run in 19 September 2008, LHC was upgraded to avoid further problems, and is currently burning all world collision energy records: on 8-14-16th of December 2009 provided collision at 2.36 TeV (Tevatron provides 1 TeV collisions), on 30th of March 2010, after a 2 months technical stop, reached 3.5 + 3.5 TeV collisions, on 22th of May luminosity was brought to $3 \cdot 10^{29} cm^{-2} s^{-1}$, on 26th of May design intensity bunches were brought into collision at 3.5 TeV per beam, on the end of July a 10^{12} particles multi-bunch injection was commissioned, considerably reducing the time needed to fill the LHC. Anyway, in certain conditions some instabilities are being observed with high intensity bunches in the machine, resulting in losses and reducing luminosity for physics. Those instabilities are currently under study.

2.3 Some questions about CERN

Why is CERN so important and why so many people and scientists are involved in its experiments? These are the most common questions that a person could ask about CERN and its huge facilities. Behind the answers there is all the Physics history, hundred of thousand scientists and researchers that, with their work and

theories, contributed to build up what we know about Nature nowadays. Here, a brief excerpt of the main questions is given.

The Higgs boson: Physics classifies 4 fundamental forces in Nature:

1. The Strong force: this force interaction is very strong but acts only within $10^{-13}cm$ and is responsible for holding the nuclei of atoms together.
2. The Weak force: this force is responsible for radioactive decay and neutrino interactions. It acts within a very short range and is the weakest force.
3. The Gravitational force: this force is very long range, always attractive having in mass its source, but very weak (for this reason it is negligible in high energy experiments).
4. The Electromagnetic force: this force is responsible for charged particles interaction and magnetic phenomena. It is repulsive or attractive and long ranged.

In the Standard Model (ST), strong, weak and electromagnetic forces result from exchange of force-carriers named bosons, (respectively gluons, W and Z bosons, photons). At the basis of the ST there is the unification of weak and electromagnetic force in the electroweak force. In order for this unification to work mathematically, force-carriers should have no mass, but from experiments this is not true. Peter Higgs, Robert Brout and Francois Englert, proposed the existance of a Higgs field and a Higgs boson which particles interact with acquiring mass. The mass of the Higgs boson is known in a certain range of energy, for this reason many scientists expect to find the Higgs boson, or at least "something else", in the LHC experiments that should finally complete the search range.

Anti-matter: It is well known from theory and experiments that electron and positron annihilate when colliding one against each other. It is also common experience that in the every day life we deal with matter, not anti-matter. Experiments at CERN will try to enlighten this tiny preference of Nature.

String theory: The String Theory substitutes the typical point like elementary particle with a vibrating string. A consequence of this model is the enlargement to multidimensional spaces. For instance, one could explain the weakness of the gravity force in comparison with other forces, considering a "weak" projection on our 3D world. Experiments like LHC could really open new dimensions on this theory.

Experiments at CERN, in particular LHC, could answer to these and many other questions, or, as often happens, just give us another route to investigate.

2.4 The accelerators chain

An accelerator is a machine that could help scientists answering the above mentioned questions. At the time this thesis is written, LHC is increasing its luminosity week by week, and many people are waiting for first experiments' results. To reach the high energy of 3.5 TeV, a beam has to pass a chain of accelerators and to be manipulated

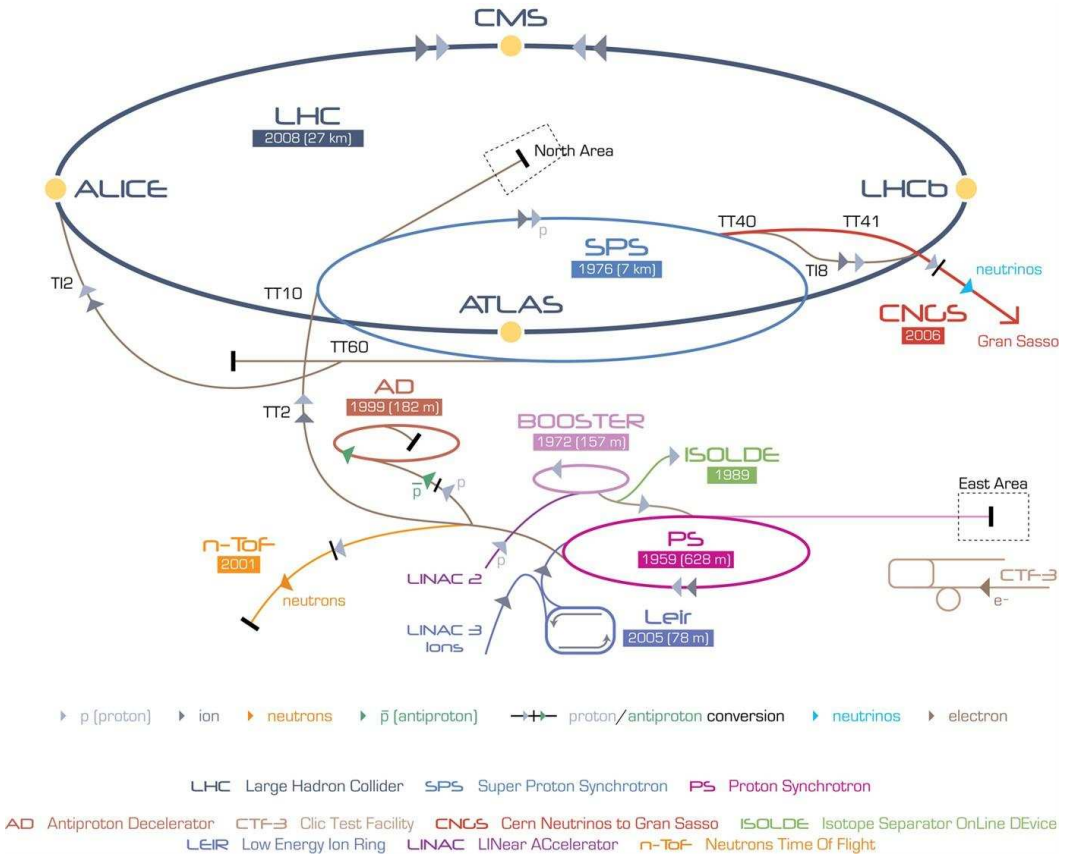

Figure 2.1: CERN accelerator complex

in order to have the right shape in term of emittance and bunch length. In Figure 2.1 we can have a look of the accelerators chain at CERN. A brief description of the LHC beam route follows.

LINAC2 Hydrogen atoms are taken from a standard hydrogen bottle, then protons are obtained by stripping electrons off atoms. Protons produced with a kinetic energy of 100 keV are injected in a RF Quadrupole where they are focused and accelerated at the same time. When they reach 750 keV they are injected in LINAC2, a linear accelerator, where they get 50 MeV energy at extraction.

PSB Protons are injected in the PSB (Proton Synchrotron Booster), a particular accelerator built in 1972 with four rings superimposed. Here the beam reaches 1.4 GeV top energy.

PS Built in 1972, the Proton Synchrotron is the oldest machine at CERN and, in its long working experience, managed many different kind of particles: protons, antiprotons, electrons, positrons and various species of ions. It injects the beam in SPS at 25 GeV via TT2 and TT10 transfer lines.

SPS The Super Proton Synchrotron is a circular proton accelerator with a circumference near 7 Km. SPS was used also as a proton - antiproton collider, making possible in 1983 the W and Z bosons discovery. Here the beam is accelerated up to 450 GeV/c, ready to be injected in LHC via TT60/TI2 and TT40/TI8 transfer lines.

LHC The beam coming from SPS is injected in the 27 Km long Large Hadron Collider. The clockwise and anticlockwise bunches reach 3.5 TeV energy under normal operating conditions and collide in one of the four Interaction Points (IPs) where huge detectors are positioned. At nominal working conditions, the machine will host 2808 25ns-spaced, 1.12ns-long bunches, each one with an intensity of $1.15 \cdot 10^{11}$ protons per bunch, in order to reach a peak luminosity of $10^{34} cm^{-2} s^{-1}$.

2.5 CERN complex upgrade

In this section we will give an insight in the future developments to the CERN accelerator complex. We will focus, mainly, on the motivations behind the LHC upgrade, that leads all the accelerator chain as a consequence [3] [4].

2.5.1 Motivations

The main motivation that leads to upgrade all the CERN accelerator complex is economical: the LHC is a significant public investment for pursuing the research in high-energy physics and the origin of Universe. For this reason, whatever can reasonably be done to reach high performance limits, should be taken into account, keeping in mind the required development time for new concepts and new technologies.

The number of events one could study in a collider, are directly correlated with the *Luminosity* parameter. Luminosity is *rate of events* normalized on *cross section* ($[L] = s^{-1} cm^{-2}$). In order to significantly change the LHC physics, a factor 10 increment in luminosity and/or an energy upgrade to 28 TeV is required. This will allow scientists to access new high-mass frontiers and to make precision measurement of rare processes (for instance, the Higgs, Supersymmetry and Extra Dimension sectors have cross-sections which rise rapidly with energy).

2.5.2 LHC upgrade

The final LHC conceptual design provides a challenging machine optimised for a nominal luminosity of $10^{34} s^{-1} cm^{-2}$ at 7 TeV beam energy. In order to improve this machine performance, the objective is to reach 10 times the luminosity and double the beam energy.

If we consider short bunches with $\sigma_z \ll \beta^*$ where β^* is the beta function at the interaction point and σ_z the 1-sigma rms bunch length, the peak luminosity can be expressed as:

$$L = \frac{N_b^2 n f_{rev}}{4\pi \sigma^{*2}} F \tag{2.1}$$

where N_b is the number of particles per bunch, n is the number of bunches, $\sigma^* = \sqrt{\varepsilon \beta^*}$ the transverse beam size, F is the reduction factor dependent from optics and bunch parameters. As one can see, higher luminosity can be obtained increasing the number of particles in bunches, the number of bunches themselves reducing the bunch spacing, decreasing the β^* at IPs and the emittance ε.

In the following we report a brief description of some limitations that are currently being analyzed and optimized.

1 The so called *dynamic aperture* defines the maximum stable amplitude of single particle betatron oscillation and it is obtained from magnetic field quality and lattice correctors studies. The long range beam-beam interaction reduces it and fixes the lower bound for the beam separation at injection.

2 The *single beam intensity* is limited by collective effects both in LHC and the injection complex, and by other damping mechanisms. Fixing the bunch spacing to new smaller values, the main limit could be caused by electron cloud effects.

3 Space charge limits *transverse beam emittance* ε in the injection complex and then the final beam brillance, as in proton machines beam emittance can only increase (in lepton machine, synchrotron radiation reduces it).

4 The *luminosity lifetime* is limited by the rate of nuclear interaction between the two beams and the rest of gas, and mechanisms governing transverse beam size and intensity, like intra-beam scattering, beam-beam interactions, damping caused by synchrotron radiation and electron cloud.

The LHC upgrade has been divided in three phases in order to gradually allow technology improvements and further researches: phase 0, where will be reached maximum performances without hardware changes, phase 1, where only LHC arcs will be kept unchanged, phase 2, where major hardware changes are planned (for example, to install new superconducting magnets in LHC to reach beam energy around 12.5 TeV). This is a temporary upgrade plan, depending on the current performance of the machine.

Chapter 3

Transverse plane instabilities

The purpose of this chapter is to give the reader an insight in wake field and impedances. This topic is part of the wider collective effects and instabilities theory in accelerators: year by year, researches and studies are performed in order to increase instability thresholds and make new higher intensity experiments achievable.

In the following we start treating the direct space charge effect, even if it is retained negligible in SPS [5], then we introduce wake fields and impedances, focusing the attention on detuning and driving components, finally we analyse the effects of such instabilities on beam dynamics and, in particular, in the SPS machine.

3.1 Space charge

A beam is a "collection" of equally charged particles traveling in a beampipe. In a first approach, one can immediately understand that repulsive forces inside the bunch are going to perturb the design single particle motion [6] [7].

The space charge (SC) effect takes its origin from Lorentz's law:

$$\vec{F_l} = q(\vec{E} + \vec{v} \times \vec{B}) \tag{3.1}$$

with $\vec{E}$ and $\vec{B}$ respectively the electric and magnetic field, q the particle charge and $\vec{v}$ the particle's velocity. Considering two particles equally charged moving in the same direction $\vec{z_0}$ with a velocity v, one can calculate the Lorentz force experienced by one of them, simply applying Lorentz transformations from the particle's frame (S') to the laboratory frame (S):

$$E'_x = \gamma(E_x - vB_y), \tag{3.2}$$
$$E'_y = \gamma(E_x + vB_x), \tag{3.3}$$
$$E'_s = E_s, \tag{3.4}$$
$$B'_y = \gamma(B_y + \frac{v}{c^2}E_x), \tag{3.5}$$
$$B'_x = \gamma(B_x - \frac{v}{c^2}E_y), \tag{3.6}$$
$$B'_s = B_s. \tag{3.7}$$

Being $\vec{B}' = 0$ in S' one can use (3.5) and (3.2) obtaining:

$$F_x = qE_x(1 - \beta^2) = q\frac{E_x}{\gamma^2}. \tag{3.8}$$

It is interesting to notice that, increasing relativistic γ, the magnetic field leads to reducing the total force acting on the particles.

As this force acts for every particle in a bunch, then it is interesting to evaluate it in the whole bunch. Considering an infinitely long, homogeneous bunch with given length l in a cylinder of radius a in a beam pipe of radius b traveling in the $\vec{z}_0$ direction, one can obtain the total force by applying the Gauss law

$$\int_S \vec{E} \cdot \vec{n}_0 \, dS = \frac{1}{\epsilon_0} \int_V \rho \, dV,$$

where ρ is the volume charge density in the cylinder given by $\rho = Q/(\pi a^2 l)$ with Q total beam charge. Applying equation (3.8) in cylindrical coordinates to the resulting electric field, one gets [8]:

$$F = \frac{q}{\gamma^2} \frac{\lambda}{2\pi\epsilon_0} \frac{1}{r}, \qquad a < r < b \tag{3.9}$$

$$F = \frac{q}{\gamma^2} \frac{\lambda}{2\pi\epsilon_0} \frac{r}{a^2}, \qquad r < a \tag{3.10}$$

with $\lambda = Q/l$. Equation (3.10) explains the SC defocusing action: since the force is always positive, SC is defocusing. In a quadrupole, on the contrary, one has an attracting force in one plane, and repulsive in the other.

Let's look at the effect on the transverse particle motion. This is governed by [7]:

$$z''(s) + K_z(s) z(s) = \frac{F^{pert}}{\beta^2 E_{tot}}, \tag{3.11}$$

with $z = [x, y]$, F^{pert} the perturbing force, E_{tot}, total beam energy, $K_z(s)$ quadrupolar strength, $z''(s)$ second derivative respect to s. Substituting the (3.10) slightly modified for a gaussian bunch, the (3.11) becomes:

$$z''(s) + K_z(s) z(s) = \frac{q^2 \lambda}{4\pi\epsilon_0 \gamma^2 \beta^2 E_{tot} \sigma_z^2} z(s), \tag{3.12}$$

Moving the r.h.s to the l.h.s. as a linear tune perturbation, one gets:

$$z''(s) + (K_z(s) + \Delta K_z) z(s) = 0 \tag{3.13}$$

from which one obtains the SC tune spread:

$$\Delta Q_z = \frac{1}{4\pi} \int_0^{2\pi R} \Delta K_z \beta(s) \, ds \simeq -\frac{e}{8\pi\epsilon_0} \frac{\lambda R}{\beta\gamma E \epsilon_{N,z}^{rms}} \tag{3.14}$$

with $\epsilon_{N,z}^{rms}$, normalised emittance equal to $\epsilon_z \beta\gamma$.

Using the table given in A , one can compute from (3.14) a maximum tune spread $\Delta Q_z \simeq -0.05$.

3.2 Wake fields and impedances

A beam travelling in a beam-pipe can be seen like a source current that excites electromagnetic (em) fields inside the structure. In order to have a physical insight in what a *wake field*, or simply a *wake*, is, we present two cases: a beam travelling in a resistive-wall beam-pipe, and a beam passing in a cavity-like structure [12].

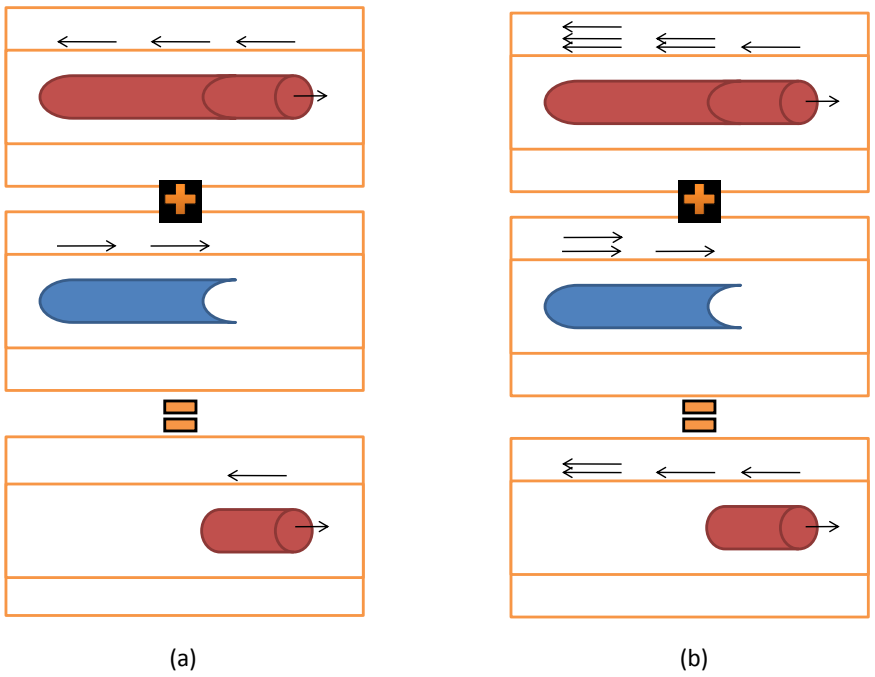

Figure 3.1: Intuitive explanation of finite conductivity in a pipe (in red positive charged particles, in blue negative charged ones). In a perfect conductor currents stay confined on the surface and the image currents follow the beam (case a), in a finite conductivity pipe currents penetrate and give result to a wake field (case b)

Resistive wall: when a beam travels in a beam-pipe, currents are induced in the walls. If the wall conductivity is virtually infinite, the induced currents stay confined to the surface following the beam movement. If the wall conductivity is finite, as in the real case, currents are going to penetrate in the wall material and excite em fields behind the bunch. The width of penetration, or "skin depth", is given by $\delta = \sqrt{\frac{2}{\omega \mu_r \sigma}}$. In Figure 3.1 these two cases can be reconstructed looking at a bunched beam like a net result of two infinitely long bunches, one longer positively charged, one shorter negatively charged: in case of finite conductivity, the positive charged beam's currents have "more time" to penetrate in the walls, only part of their effect will be canceled by the opposite currents generated by the negative charged beam; in case of infinite conductivity, currents stay confined to the surface and ideally perfectly cancels overlapping positive and negative beam's ones, the current follows the bunch not giving rise to any wake field.

Cavity: in Figure 3.2 a beam current I_b excites a magnetic field in the cavity. Taking into account only the TM_{010} excited mode in which magnetic field is azimuthal around the beam direction, a surface current I_s flows in the cavity walls to oppose the magnetic field built up by the beam. This current transports charges from one side of the cavity to the other creating a displacement current I_c induced by the increasing electric field between the cavity's plates. This

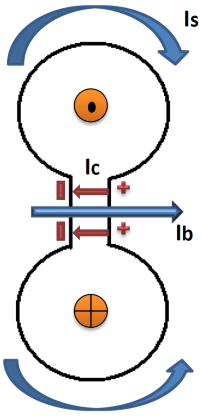

Figure 3.2: Intuitive explanation of how a resonant wake field is built up by beam current passing. I_b is the beam current that excites I_s, surface current, and I_c, displacement current

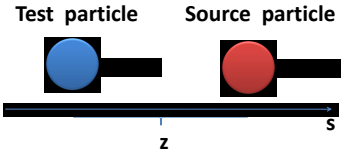

Figure 3.3: Source and test charge relative positions are $s_{test} = s_{source} + z$. Here we assume $z < 0$

picture can be drawn also for other cavity modes. Each mode oscillates in the cavity with a quality factor given by the conductivity of the walls. It follows that one has to damp these modes if undesired, specially if they are excited by discontinuities between different elements in an accelerator (i.e. beam-pipe to pumping ports transitions). For this reason, materials with low conductivity are used (like ferrites) or shielding.

In both cases, an electric and magnetic field is created in the structure. As we will see in the next section, these beam induced fields couple with the beam by changing momentum of its particles.

3.2.1 Multipolar decomposition

Now we introduce the wake field concept starting from a problem: determine the momentum change for a test particle following a source particle travelling in a cylindrical beam pipe [13], [14], [8]. In Figure 3.3 the position of source and test particle is given by:

$$s_{test} = s_{source} + z, \tag{3.15}$$

$$s_{source} = \beta ct. \tag{3.16}$$

with $z < 0$. In order to simplify our problem we will do two assumptions:

1. **Rigid beam approximation:** we will suppose that the distance z between test and source particle remains constant during the wake field perturbation.

2. **Impulse approximation:** since the test particle moves with constant velocity βc we will study the change in its momentum after the whole interaction. In a certain point of view we are substituting a *distributed* interaction with a *lumped* one. The expression of momentum change is in fact given by this integration:

$$\Delta\vec{p}(x,y,z) = \int_{-\infty}^{\infty} \vec{F}(x,y,s=z+\beta ct,t)\,dt \tag{3.17}$$

$$= \int_{-\infty}^{\infty} e(\vec{E}+\vec{v}\times\vec{B})\,dt \tag{3.18}$$

Since we want to calculate $\Delta\vec{p}$ it will be useful to apply the *Panofsky-Wenzel theorem* which states, in our hypothesis, the following relationship:

$$\vec{\nabla}\times\Delta\vec{p}(x,y,z) = 0. \tag{3.19}$$

Adding the $\beta = 1$ hypothesis and calculating $\vec{\nabla}\cdot\vec{F}$ one gets:

$$\vec{\nabla}_\perp\cdot\Delta\vec{p}_\perp(x,y,z) = 0. \tag{3.20}$$

Including the cylindrical geometry information, equations (3.19) and (3.20) simplifies to:

$$\frac{1}{r}\left(\frac{\partial\Delta p_z}{\partial\theta}\right) = \frac{\partial\Delta p_\theta}{\partial z}, \tag{3.21}$$

$$\frac{\partial\Delta p_r}{\partial z} = \frac{\partial\Delta p_z}{\partial r}, \tag{3.22}$$

$$\frac{\partial(r\Delta p_\theta)}{\partial r} = \frac{\partial\Delta p_r}{\partial\theta}, \tag{3.23}$$

and, with $\beta = 1$:

$$\frac{\partial(r\Delta p_r)}{\partial r} = -\frac{\partial\Delta p_\theta}{\partial\theta}. \tag{3.24}$$

The source particle can be thought like a point-like source with density $\rho(r,\theta,s,t)$. This is equal to:

$$\rho = \frac{Q}{a}\delta(r-a)\delta(\theta-\theta_0)\delta(s-vt), \tag{3.25}$$

where a is the radial displacement, $Q = eN_b$ the total charge considering the source like a macroparticle, θ_0 is the azimuthal displacement we will set to zero. The azimuthal structure symmetry permits us to develop the Dirac function in complex exponential series:

$$\delta(\theta) = \frac{1}{T}\sum_{m=-\infty}^{+\infty} e^{j2\pi m\frac{\theta}{T}} = T\sum_{m=-\infty}^{+\infty}\delta(\theta-mT) \tag{3.26}$$

Since the period is $T = 2\pi$ we have:

$$\delta(\theta) = \frac{1}{2\pi}\sum_{m=-\infty}^{+\infty} e^{jm\theta} = \frac{1}{\pi}\sum_{m=0}^{+\infty}\frac{cos(m\theta)}{1+\delta_{m0}} \tag{3.27}$$

where δ_{m0} is the Kronecker symbol. Finally one gets:

$$\rho(r,\theta,s,t) = \sum_{m=0}^{\infty} \frac{Q_m cos(m\theta)}{\pi a^{m+1}(1+\delta_{m0})}\delta(r-a)\delta(s-vt). \tag{3.28}$$

Let's write now the Maxwell's equations that govern our problem. We will study the problem in frequency domain because it will semplify the time dependency of our problem.

$$\nabla \times \vec{E} = -j\omega\mu\vec{H}, \tag{3.29}$$

$$\nabla \times \vec{H} = \rho v\vec{s} + j\omega\varepsilon_c\vec{E}, \tag{3.30}$$

$$\nabla\vec{E} = \frac{\rho}{\varepsilon_0}, \tag{3.31}$$

$$\nabla\vec{H} = 0. \tag{3.32}$$

where μ is the magnetic permeability, ε_c the complex dielectric constant. In frequency domain, the charge density ρ becomes:

$$\rho(r,\theta,s,k) = \sum_{m=0}^{\infty} \frac{Q_m cos(m\theta)}{v\pi a^{m+1}(1+\delta_{m0})}\delta(r-a)e^{jks}, \tag{3.33}$$

since $\delta(s-vt) = \mathcal{F}^{-1}\{e^{jks}/v\}$ with $k = \omega/v$.

From (3.30), substituting (3.33), one can see that, in the $\vec{s}$ direction, the electric field has to have the same current multipole dependency, and equally for Δp_z since magnetic field doesn't contribute to the momentum change in longitudinal direction. It follows that:

$$\Delta p_z = \Delta\hat{p}_z cos(m\theta), \tag{3.34}$$

and, applying (3.21) one has $\Delta p_r = \Delta\hat{p}_r cos(m\theta)$ and $\Delta p_\theta = \Delta\hat{p}_\theta sin(m\theta)$. From this one gets:

$$-\frac{m}{r}\Delta\hat{p}_z = \frac{\partial\Delta\hat{p}_\theta}{\partial z}, \tag{3.35}$$

$$\frac{\partial\Delta\hat{p}_r}{\partial z} = \frac{\partial\Delta\hat{p}_z}{\partial r}, \tag{3.36}$$

$$\frac{\partial(r\Delta\hat{p}_\theta)}{\partial r} = -m\Delta\hat{p}_r, \tag{3.37}$$

and, with $\beta = 1$:

$$\frac{\partial(r\Delta\hat{p}_r)}{\partial r} = -m\Delta\hat{p}_\theta. \tag{3.38}$$

For m=0, in (3.37) and (3.38) the r.h.s. cancels. Integrating over r we would have a singularity in $r = 0$ for $\Delta\hat{p}_r$ and $\Delta\hat{p}_\theta$, then we conclude that $\Delta\hat{p}_r = 0$ and $\Delta\hat{p}_\theta = 0$ for $m = 0$. For $m \neq 1$, from (3.37) and (3.38) we get:

$$\frac{\partial}{\partial r}\Big[r\frac{\partial(r\Delta\hat{p}_r)}{\partial r}\Big] = m^2\Delta\hat{p}_r. \tag{3.39}$$

Set $Y(r) = r\Delta\hat{p}_r$ we can develope (3.39) getting:

$$\frac{\partial^2 Y}{\partial r^2}r^2 + \frac{\partial Y}{\partial r}r + m^2 Y = 0, \tag{3.40}$$

This is an Euler-Cauchy homogeneous differential equation that can be solved substituting $Y = r^q$. The solution, neglecting constants, can be written as $\Delta\hat{p}_r \propto r^{m-1}$. From this, using (3.17) one finally gets:

$$v\Delta\hat{p}_s(r,\theta,z) = \int_0^L Fs\,ds = -qQa^m r^m cos(m\theta)W'_m(z), \tag{3.41}$$

$$v\Delta\hat{p}_r(r,\theta,z) = \int_0^L Fr\,ds = -qQa^m m r^{m-1} cos(m\theta)W_m(z), \tag{3.42}$$

$$v\Delta\hat{p}_\theta(r,\theta,z) = \int_0^L F\theta\,ds = qQa^m r^{m-1} sin(m\theta)W_m(z), \tag{3.43}$$

where the functions $W'_m(z)$ and $W_m(z)$ are respectively longitudinal and transverse *wake functions* of azimuthal mode m.

From equation (3.41) and (3.42) one can keep only first order terms for the radial dependency, obtaining:

$$W_\parallel(z) = -\frac{1}{qQ}\int_0^L F_s\,ds = -\frac{1}{Q}\int_0^L E_s\,ds, \tag{3.44}$$

$$W_\perp(z) = -\frac{1}{qQa}\int_0^L F_\perp\,ds = -\frac{1}{Qa}\int_0^L (E + v\times B)_\perp\,ds, \tag{3.45}$$

where $W_\parallel(z)$ denotes longitudinal $m = 0$ wake function and $W_\perp(z)$ the dipolar transverse $m = 1$ wake function: the first, if positive, represents a loss of energy from the source particle to the e.m. field and is measured in V/C, the second represents a transverse deflecting kick measured in $V/(C \cdot m)$. We will directly connect transverse wake to change in transverse momentum and angle in equation (3.53) and (3.56).

With this kind of analysis the force felt by a test particle has a linear dependency with the source displacement a, and no dependency on its position r. For this reason the wake component is called *driving* or *dipolar* component. In the last years, measurements and simulations on SPS components like kickers, beam position monitor, vacuum chambers, and beam-pipe revealed the necessity to include another wake component, the *detuning* or *quadrupolar* wake.

3.2.2 Dipolar and quadrupolar components

In the previous section wake fields were introduced using Chao's formalism for axisymmetric structures. In general, from the electromagnetic point of view, we have more complicated structures where the simple assumption of azimuthal symmetry is not true anymore. In the following we will define the detuning or quadrupolar wake that plays an important role for the instabilities understanding.

Let's still consider the two particles problem. Particle 1 is the source, particle 2 represents a test one. The test particle is going to *feel* a perturbing force in its transversal motion governed by:

$$\ddot{y}(t) + \omega_0^2 Q_y y(t) = \frac{F_{pert}(x_1, y_1, x_2, y_2, t = \frac{s-z}{v})}{m_0\gamma}, \tag{3.46}$$

where this time $\ddot{y}(t)$ indicates derivative over time and we choose, for example, the y-plane. Developing the r.h.s. in a first order Taylor series, i.e. perturbing y_1 and

y_2 positions, one has:

$$\ddot{y}(t) + \omega_0^2 Q_y y(t) = \frac{\frac{\partial F}{\partial y_1} y_1 + \frac{\partial F}{\partial y_2} y_2}{m_0 \gamma}, \tag{3.47}$$

where $\ddot{y}(t)$ indicates double time derivative. If we put the source particle on the design trajectory (y_1=0) and apply a little displacement y_2, from the previous equation we deduce the test particle feels a force proportional to its displacement, i.e. a detuning or quadrupolar force. If we reverse the problem, putting the test particle on the design trajectory (y_2=0) and apply a little displacement y_1 to the source, we deduce that the test particle feels a force independent by its position, i.e. a driving or dipolar force. Superposing the two effects one can study the perturbation in momentum applying first a dipolar, then a quadrupolar kick:

$$v\Delta p_y = \int_0^L F_\perp \, ds = \int_0^L (F_{dip} + F_{quad}) \, ds, \tag{3.48}$$

where:

$$F_{dip} = \frac{\partial F}{\partial y_1} y_1, \tag{3.49}$$

$$F_{quad} = \frac{\partial F}{\partial y_2} y_2. \tag{3.50}$$

Normalizing to the charges and the displacement we define the driving and detuning wake functions:

$$W_{dip} = \frac{1}{q_1 q_2 y_1} \int_0^L F_{dip} \, ds = \frac{1}{q_1 y_1} \int_0^L (E_y + v \times B_x)|_{y_2=0} \, ds, \tag{3.51}$$

$$W_{quad} = \frac{1}{q_1 q_2 y_2} \int_0^L F_{quad} \, ds = \frac{1}{q_1 y_2} \int_0^L (E_y + v \times B_x)|_{y_1=0} \, ds. \tag{3.52}$$

Wakes are measured in $V/(pCmm)$. Typical plots for quadrupolar and dipolar components are shown in Appendix A.

Now, equation (3.48) can be expressed in function of wakes:

$$v\Delta p_y = q_1 q_2 (W_{dip} y_1 + W_{quad} y_2). \tag{3.53}$$

Since, integrating, we transform a *distributed* interaction into a *lumped* one, it is common to define the wake action as a *kick* in particle momentum.

Particle motion simulators compute transverse position referring to *phase space* coordinates $(x(s), x'(s))$ and $(y(s), y'(s))$ where the derivative is respect to the longitudinal s variable in the Courant-Snyder frame (x, y, s). It is useful, for this reason, to calculate the wake field perturbation referring to $\dot{x}(s)$ and $\dot{y}(s)$ angles, in place of momentum. starting from equation (3.47) one can express time variable as $t = s/(\beta c)$ obtaining:

$$\frac{\partial^2 y_2(s)}{\partial s^2} + \frac{\omega_0^2 Q_y^2}{\beta^2 c^2} y_2(s) = \frac{F_p}{m_0 \gamma \beta^2 c^2}, \tag{3.54}$$

that leads to:

$$\frac{\partial^2 y_2(s)}{\partial s^2} + \left(\frac{Q_y}{R}\right)^2 y_2(s) = \frac{F_p}{\beta^2 E}. \tag{3.55}$$

The kick can be computed as:

$$\Delta y_2'(s) = \int_0^L y_2''(s)\, ds = \int_0^L \frac{F_y}{\beta^2 E} = \frac{q_1 q_2}{\beta^2 E}(W_{dip} y_1 + W_{quad} y_2) \tag{3.56}$$

Wakes functions can be considered like *Green* functions, since they refer to a single point-like particle modeled as a Dirac distribution in 3D space. To extend the calculation to the whole bunch, one has to do a convolution between the bunch distribution and the wake field. One has:

$$U(z) = W(z) * \lambda(z) = \int_{-\infty}^{+\infty} W(x_1, y_1, x_2, y_2, s - z)\lambda(s)\, ds. \tag{3.57}$$

Since there is no wake behind the test particle, one can extend the convolution up to $-\infty$.

3.3 Impedances

So far we have introduced a time domain approach to wake fields. Since materials are dispersive in frequency, especially if we consider ferrites, it turns to be useful to transform our results in frequency domain, defining the so called *impedances*. We define:

$$Z_\parallel(\omega) = -\int_{-\infty}^{+\infty} W_\parallel(t) e^{-j\omega t}\, dt = -\frac{1}{v}\int_{-\infty}^{+\infty} W_\parallel(z) e^{-jkz}\, dz, \tag{3.58}$$

$$Z_\perp(\omega) = \frac{j}{v}\int_{-\infty}^{+\infty} W_\perp(z) e^{-jkz}\, dz, \tag{3.59}$$

that are called respectively *longitudinal* and *transverse* impedances. The equations in (3.58) and (3.59) are used in time domain simulators like CST particle studio. Typically, in order to simplify analytical calculations, the following alternative definitions can be used. Considering now $z > 0$ we have:

$$W_\parallel(z) = \frac{1}{Q}\int_0^L E_\parallel\left(s, t = \frac{z+s}{v}\right) ds,$$

substituting in (3.58) we get:

$$Z_\parallel(\omega) = -\frac{1}{Qv}\int_{z=-\infty}^{+\infty}\left[\int_0^L E\left(s, t = \frac{z+s}{c}\right) ds\right] e^{-jkz}\, dz.$$

Inverting integrals and passing from space z to time t variable, we have:

$$Z_\parallel(\omega) = -\frac{1}{Q}\int_0^L\left[\int_{z=-\infty}^{+\infty} E\left(s, \frac{t+s}{c}\right) e^{-j\omega t}\, dt\right] ds,$$

that leads to:

$$Z_\parallel(\omega) = -\frac{1}{Q}\int_0^L E(s,\omega) e^{jks}\, ds. \tag{3.60}$$

A similar procedure can be followed to obtain transverse impedance:

$$Z_\perp(\omega) = \frac{j}{Q}\int_0^L (\vec{E}(s,\omega) + \vec{v}\times\vec{B})|_\perp e^{jks}\, ds. \tag{3.61}$$

Dipolar and quadrupolar impedances can be easily obtained either Fourier-transforming respective wakes, or applying (3.60) and (3.61) to the em. fields. An example of kicker's impedance is shown in Figure 3.4

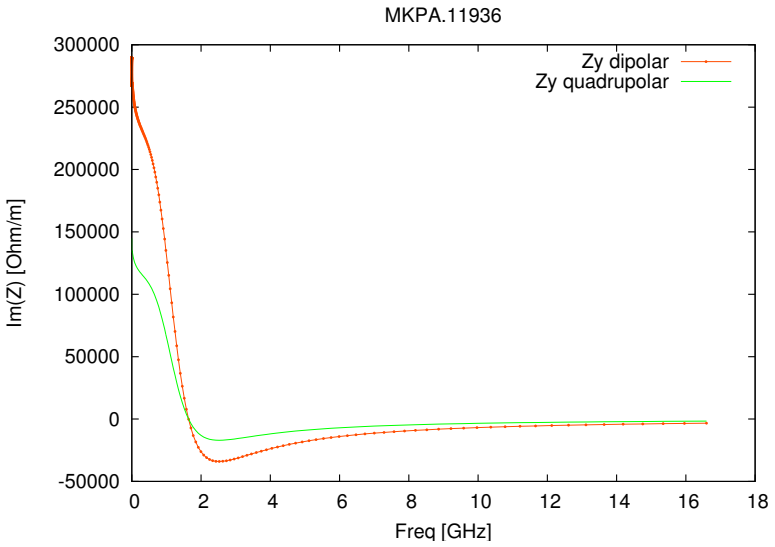

Figure 3.4: Dipolar and Quadupolar vertical impedance for the injection kicker MKPA.11936

3.4 Some example of impedance and wake's calculation

So far we have seen two different approaches to wake field's calculation: time domain (TD) and frequency domain (FD). The former uses (3.44) for the longitudinal wake, (3.51) and (3.52) for dipolar and quadrupolar one, and is typically implemented in TD solver like CST particle studio, the latter uses (3.60) and (3.61) to compute respectively longitudinal and transversal, dipolar or quadrupolar, impedances, and is very useful for analytical calculation. In this section we briefly report two interesting examples about FD impedances calculation: a cylindrical and a flat geometry. The first one represents the beam pipe structure, the second one a kicker, one of the most important contributors to the SPS impedance.

3.4.1 Cylindrical geometry

The complete description of this problem can be found in [15]. Here we will mainly focus the attention over the steps one has to complete in order to get the multilayer cylindrical beam pipe impedance.

Let's consider a point like source beam at position $\theta = 0$, $s = vt$, $r = a_1$, travelling along the axis of an axisymmetric infinitely long pipe of inner radius b and p layers, as shown in Fig. 3.5. The source charge can be decomposed like in (3.33). Developing Maxwell equations one gets, for the electric field:

$$\nabla^2 \vec{E} + k^2 \vec{E} = j\omega\mu\rho v + \nabla\left(\frac{\rho}{\varepsilon_0}\right) \tag{3.62}$$

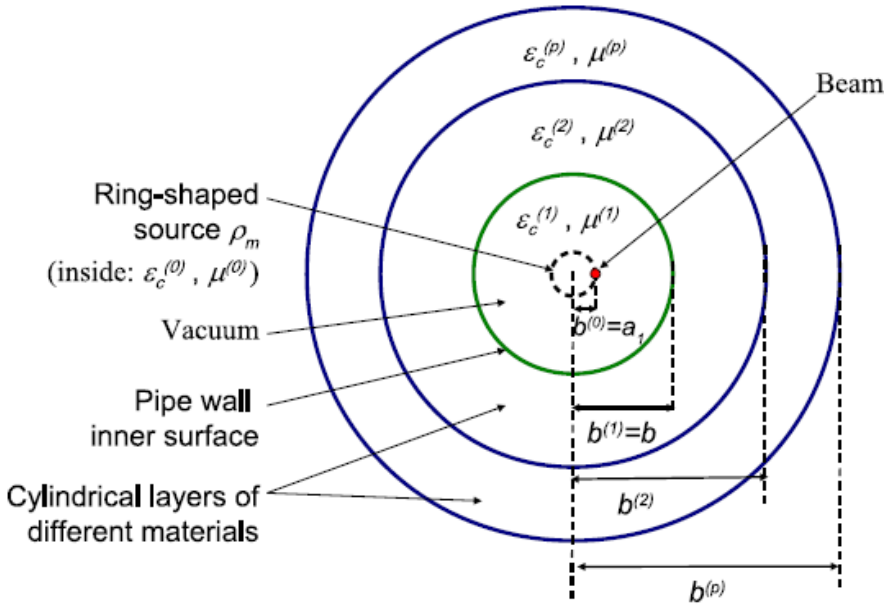

Figure 3.5: Multi-layered cylindrical beam pipe. Courtesy of E.Metral, N.Mounet

Since transverse field components depend on longitudinal ones, we can expand Laplace operator and divergence operators for cylindrical coordinates in the longitudinal direction. We get:

$$\left(\frac{1}{r}\frac{\partial}{\partial r}\left(r\frac{\partial}{\partial r}\right)+\frac{1}{r^2}\frac{\partial^2}{\partial\theta^2}+\frac{\partial^2}{\partial s^2}+k^2\right)E_s = j\omega\mu\rho_m+\frac{1}{\varepsilon_0}\frac{\partial\rho_m}{\partial s} \tag{3.63}$$

and analogous for H_s longitudinal magnetic field. The right side forcing term is null away from the source. Solving for separation of variable, we can develop $E_s(r,\theta,s) = R(r)\Theta(\theta)exp(-jk_s s)$ where $\Theta(\theta)_E = cos(m\theta)$ for the electric field and $\Theta(\theta)_E = sin(m\theta)$ for magnetic field. Equation (3.63) becomes a modified Bessel differential equation that leads to:

$$E_s = cos(m\theta)e^{-jk_s s}\left[C_{Ie}I_m(\nu r)+C_{Ke}K_m(\nu r)\right], \tag{3.64}$$

$$H_s = Z_0^{-1}sin(m\theta)e^{-jk_s s}\left[C_{Ih}I_m(\nu r)+C_{Kh}K_m(\nu r)\right] \tag{3.65}$$

where $I(\nu r)$ and $K(\nu r)$ are modified Bessel functions, with $\nu = \sqrt{k_s^2-k^2}$ and $C_{I,K}$ constants depending on mode m and frequency ω. These fields can be obtained for each layer p^{th} leading to $2\times p$ longitudinal equations with $4\times p$ constants. Part of them can be calculated considering matching conditions with the source charge and finiteness of the field for $r\to 0$ and $r\to\infty$. Moreover, it can be shown that $\vec{C}_{K,I}^{p+1} = M_p^{p+1}\times\vec{C}_{K,I}^{p}$ that leads to iterative calculations in order to fix all the constants.

Having the E_s and H_s fields one can compute easily also transverse components [13] and then, finally, calculate the impedances using (3.60) and (3.61). Displacing

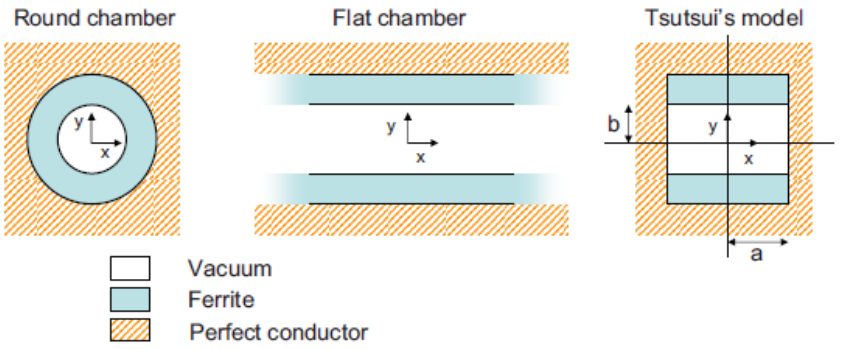

Figure 3.6: Various kicker's model: (a) Cyrcular shape; (b) Infinite plats loaded with ferrite slabs; (c) Ferrite slab loaded wave guide. Courtesy of E.Metral et al.

a test particle to $\theta = \theta_2$ and $r = a_2$ one has:

$$Z_{\parallel}(\omega) = -\frac{1}{Q}\int_0^L E_s(a_2, \theta_2, s; \omega) e^{jks}\, ds, \tag{3.66}$$

$$Z_x(\omega) = \frac{j}{Q}\int_0^L (E_x(a_2, \theta_2, s; \omega) + v\mu H_y(a_2, \theta_2, s; \omega)) e^{jks}\, ds. \tag{3.67}$$

The important result we want to underline is that, solving these equations one can obtain the wall impedances to any order in a_1 and a_2. The first order terms are shown below and we clearly recognize the presence of a quadrupolar impedance (term proportional to a_2).

$$Z_{dip} = \frac{jLZ_0k^2}{4\pi\beta\gamma^4}\alpha_{TM}a_1 \tag{3.68}$$

$$Z_{quad} = \frac{jL\mu\omega}{4\pi\beta^2\gamma^4}\alpha_{TM}a_2 cos(\theta_2) \tag{3.69}$$

3.4.2 Flat geometry

The complete description of this problem can be found in [19] [17]. Our purpose, in this section, is to give an outlook in impedances calculations in flat geometries.

A flat geometry can model a kicker, the element used to kick the beam in order to measure the tune, inject, extract from the ring, dump the beam itself.

In Fig. 3.6 different geometries are presented, typically used to compute wake fields and impedances for this element. A first approximation consist in compute wakes in a circular structure (a) then use Yokoya factors [20] to scale to a flat geometry (b). A new geometry, closer to the real kicker's shape is presented in (c) and was studied by H.Tsutsui (dipolar wakes) in [16] and B.Salvant (quadrupolar wakes) in [18].

Referring to (c) we have a rectangular wave guide of width $2a$ and height $2d$, partially filled with two symmetrical ferrite slabs with ε_r, μ_r. The beam passes through the structure's center at $\pm b$ height. Because to the traslational simmetry, vector potential $\vec{A}(x, y, z)$ can be decomposed in longitudinal $L(z)$ and transverse

$T(x,y)$ components. For TE modes we have:

$$A(z) = T(x,y)\left[L_0^+ e^{-jk_z z} + L_0^- e^{+jk_z z}\right] \tag{3.70}$$

In each region we have to solve the transverse Helmholtz equation $\nabla_t^2 T(x,y) + k_t^2 T(x,y) = 0$ to compute the fields in the structure. These can be divided in TE and TM modes whose field components are:

$$\vec{E}_t^{TE} = L(z)\vec{z}_0 \times \nabla_t T^{TE}(x,y), \tag{3.71}$$

$$E_z^{TE} = 0, \tag{3.72}$$

$$\vec{H}_t^{TE} = \frac{1}{j\omega\mu}\frac{L(z)}{z}\nabla_t T^{TE}(x,y), \tag{3.73}$$

$$H_z^{TM} = \frac{k_t^2}{j\omega\mu}T^{TE}(x,y)L(z). \tag{3.74}$$

with boundary condition at the perfect conducting border:

$$\frac{\partial T^{TE}}{\partial \vec{n}} = 0. \tag{3.75}$$

For TM modes we have:

$$\vec{H}_t^{TM} = L(z)\nabla_t T^{TM}(x,y) \times \vec{z}_0, \tag{3.76}$$

$$H_z^{TM} = 0, \tag{3.77}$$

$$\vec{E}_t^{TM} = \frac{1}{j\omega\varepsilon}\frac{L(z)}{z}\nabla_t T^{TM}(x,y), \tag{3.78}$$

$$E_z^{TM} = \frac{k_t^2}{j\omega\varepsilon}T^{TM}(x,y)L(z). \tag{3.79}$$

with boundary condition at the perfect conducting border:

$$T^{TM} = 0. \tag{3.80}$$

Also in this case, we can solve the Helmholtz equation by separation of variables: $T(x,y) = X(x)Y(y)$. Substituting the last expression in the Helmholtz equation, one gets:

$$\frac{\partial^2}{\partial x^2}X(x)Y(y) + \frac{\partial^2}{\partial y^2}X(x)Y(y) + k_t^2 X(x)Y(y) = 0 \tag{3.81}$$

that is valid for both cases, TE and TM. A generical solution for $X(x)$ and Y(y) can be found derivating the (3.81) over x and y. We then get the harmonic motion differential equation that leads to the following general solutions:

$$X(x) = A_1 sin(k_x x) + B_1 cos(k_x x) \tag{3.82}$$

$$Y(y) = A_2 sin(k_y y) + B_2 cos(k_y y) \tag{3.83}$$

Let's consider, first, TM modes. Boundary conditions in the upper side ferrite slab are given by (3.80) and lead to:

$$X(x)\Big|_{x=[0;2a]} = 0 \tag{3.84}$$

$$Y(y)\Big|_{y=[d]} = 0 \tag{3.85}$$

$$\tag{3.86}$$

Since we have a π radiants rotation symmetrical structure around z, we can only accept even solution in x for electric field. The $X(x)$ solution, then, can only be:

$$X(x) = B_n cos(k_{xn} x) \tag{3.87}$$

with $k_{xn} = \frac{\pi}{2a}(1 + 2n)$. Solving also for the y direction, we get:

$$E_z = \frac{k_{t_n}^2}{j\omega\varepsilon} B_n cos(k_{x_n} x) sin(k_{y_n}(y - d)) \tag{3.88}$$

where k_{yn} will be fixed by the matching condition at $y = b$. Using (3.76) one gets:

$$E_x^{TM} = \frac{k_z}{\omega\varepsilon} B_n k_{x_n} sin(k_{x_n} x) sin(k_{y_n}(y - d)) \tag{3.89}$$

$$E_y^{TM} = \frac{-k_z}{\omega\varepsilon} B_n k_{y_n} cos(k_{x_n} x) cos(k_{y_n}(y - d)) \tag{3.90}$$

$$H_y^{TM} = B_n k_{x_n} sin(k_{x_n} x) sin(k_{y_n}(y - d)) \tag{3.91}$$

$$H_x^{TM} = B_n k_{y_n} cos(k_{x_n} x) cos(k_{y_n}(y - d)) \tag{3.92}$$

where we implied the $e^{jk_z z}$ longitudinal z dependence.

We use the same procedure for TE fields. Using (3.75) one gets:

$$\frac{\partial X}{\partial x} \Big|_{x=[0;2a]} = 0 \tag{3.93}$$

$$\frac{\partial Y}{\partial y} \Big|_{y=[d]} = 0 \tag{3.94}$$

The longitudinal magnetic field is:

$$H_z = \frac{k_{t_n}^2}{j\omega\mu} A_n sin(k_{x_n} x) cos(k_{y_n}(y - d)) \tag{3.95}$$

Using (3.71) one gets:

$$H_x^{TE} = -\frac{k_z}{\omega\mu} A_n k_{x_n} cos(k_{x_n} x) cos(k_{y_n}(y - d)) \tag{3.96}$$

$$H_y^{TE} = \frac{k_z}{\omega\mu} A_n k_{y_n} sin(k_{x_n} x) sin(k_{y_n}(y - d)) \tag{3.97}$$

$$E_y^{TE} = A_n k_{x_n} cos(k_{x_n} x) cos(k_{y_n}(y - d)) \tag{3.98}$$

$$E_x^{TE} = A_n k_{y_n} sin(k_{x_n} x) sin(k_{y_n}(y - d)) \tag{3.99}$$

The final *Tsutsui* fields' expressions can be obtained summing TE and TM modes considering the same $k_z = \omega\sqrt{\mu_0\mu_r\varepsilon_0\varepsilon_r}$ propagation constant and using these two following relationships for constants:

$$C_n = \frac{k_{t_n}^2 B_n}{j\omega\varepsilon} \tag{3.100}$$

$$D_n = \frac{k_{t_n}^2 Z_0 A_n}{j\omega\mu} \tag{3.101}$$

Eventually one gets:

$$Z_0 H_z = \sum_{n=0}^{\infty} H_{z_n}^{TE} = \sum_{n=0}^{\infty} D_n sin(k_{x_n} x) cos(k_{y_n}(y-d)) \tag{3.102}$$

$$Z_0 H_x = \sum_{n=0}^{\infty} H_{x_n}^{TE} + H_{x_n}^{TM} = \tag{3.103}$$

$$= \frac{j}{\varepsilon_r \mu_r - 1} \sum_{n=0}^{\infty} \left(\varepsilon_r \frac{k_{y_n}}{k_0} C_n - D_n \frac{k_{x_n}}{k_0} \right) cos(k_{x_n}) cos(k_{y_n}(y-d)) \tag{3.104}$$

$$Z_0 H_y = \sum_{n=0}^{\infty} H_{y_n}^{TE} + H_{y_n}^{TM} = \tag{3.105}$$

$$= \frac{j}{\varepsilon_r \mu_r - 1} \sum_{n=0}^{\infty} \left(\varepsilon_r \frac{k_{x_n}}{k_0} C_n - D_n \frac{k_{y_n}}{k_0} \right) sin(k_{x_n}) sin(k_{y_n}(y-d)) \tag{3.106}$$

$$E_z = \sum_{n=0}^{\infty} E_{z_n}^{TM} = \sum_{n=0}^{\infty} C_n cos(k_{x_n} x) sin(k_{y_n}(y-d)) \tag{3.107}$$

$$Ex = \sum_{n=0}^{\infty} E_{x_n}^{TE} + E_{x_n}^{TM} = \tag{3.108}$$

$$= \frac{j}{\varepsilon_r \mu_r - 1} \sum_{n=0}^{\infty} \left(\frac{k_{x_n}}{k_0} C_n + \mu_r D_n \frac{k_{y_n}}{k_0} \right) sin(k_{x_n}) sin(k_{y_n}(y-d)) \tag{3.109}$$

$$Ey = \sum_{n=0}^{\infty} E_{y_n}^{TE} + E_{y_n}^{TM} = \tag{3.110}$$

$$= \frac{j}{\varepsilon_r \mu_r - 1} \sum_{n=0}^{\infty} \left(\frac{-k_{y_n}}{k_0} C_n + \mu_r D_n \frac{k_{x_n}}{k_0} \right) cos(k_{x_n}) cos(k_{y_n}(y-d)) \tag{3.111}$$

In the vacuum region, the solution to (3.81) is similar except for the $Y(y)$ function. Since we have a symmetrical structure, we get:

$$Y(y) = A_n cos(k_{y_n} y) \tag{3.112}$$

Propagation constant k_z has to be the same of ferrite slabs in order to satisfy boundary conditions. From separability condition we have:

$$k_{y_n}^2 = k_0^2 - k_{z_n}^2 - k_{x_n}^2 = -k_{x_n}^2 \rightarrow k_{y_n} = j k_{x_n} \tag{3.113}$$

The (3.112), then, transforms in a hyperbolic cosine:

$$Y(y) = A_n cosh(k_{x_n} y) \tag{3.114}$$

Like in the cylindrical case, we can compute dipolar and quadrupolar wake fields displacing the source and test particles. In this work we will use a simplified set of kickers wake fields computed with Yokoya factors from a cylindrical geometry (see Appendix B). In this approximation, the dipolar impedance calculated for a circular

beam pipe is transformed using the following factors:

$$Z_y^{dip} = \frac{\pi^2}{12} Z_{cyrc} \tag{3.115}$$

$$Z_x^{dip} = \frac{\pi^2}{24} Z_{cyrc} \tag{3.116}$$

$$Z_y^{quad} = \frac{\pi^2}{24} Z_{cyrc} \tag{3.117}$$

$$Z_x^{quad} = -\frac{\pi^2}{24} Z_{cyrc}. \tag{3.118}$$

Chapter 4

Impedance detection in SPS

In this chapter we will analyze the effects of impedance in a global and local point of view. The Sacherer formula will be reported for the global observables, and the phase advance beating formula will be fully derived. These will be used to describe the SPS impedance at the date this thesis is written. Tracking simulator code *HEADTAIL* and lattice design tool *MAD-X* will be then presented in order to complete the following detecting algorithm description.

4.1 Transverse motion observables

As we have seen in equation 3.47 we can study wake field effects adding their perturbation on the right side in the Hill's equation. This effect globally acts as a tune shift that can be quantified using Sacherer's formula for a gaussian bunch [9], [11]:

$$\Delta Q = \frac{N_b e^2 c}{4\sqrt{\pi}\omega_0\omega_\beta E T_0 \sigma_t} Im(Z_\perp)_{eff} \tag{4.1}$$

where N_b is the number of particle in the bunch, E is the energy, T_0 the revolution time period, $\sigma_t = \sigma_z/c$ the rms bunch length, $\omega_\beta = Q\omega_0$ with Q the nominal tune, $Im(Z_\perp)_{eff}$ the imaginary part of effective impedance given by the convolution between the impedance and the longitudinal bunch spectrum:

$$Z_\perp(\omega_\xi)_{eff} = \int_{-\infty}^{+\infty} Z_\perp(\omega') h_0(\omega' - \omega_\xi)\, d\omega' \tag{4.2}$$

with

$$h_0(\omega) = \frac{\sigma_t}{\sqrt{\pi}} e^{-(\omega\sigma_t)^2} \tag{4.3}$$

The Gaussian bunch spectrum is centered in $\omega_\xi = \xi\frac{\omega_\beta}{\eta}$ with ξ the chromaticity and η the slippage factor. This derivation is valid in the intensity range for which the tune shift with intensity is linear. In term of intensity threshold, for SPS, this means $N_b < 8 \cdot 10^{10}$ [22].

There are at least two implications from equation (4.1):

1 - It avails us to measure the total effective impedance in accelerator rings, measuring tune shift as a function of intensity (we will show some example in the following section).

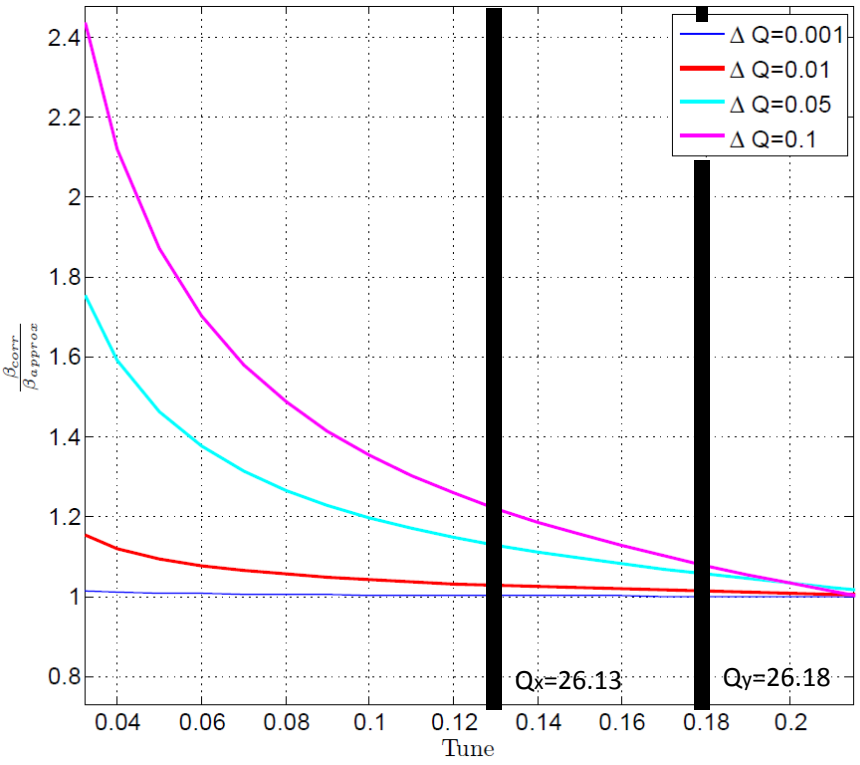

Figure 4.1: Ratio between correct beta beating due to single quadrupolar error and first order approximation formula.

.

2 - It avails to detect local sources of impedances. From optics theory, it is well known that a quadrupole error induce a local beta-beating and a tune shift. In linear approximation, for a given intensity, one can compute the tune shift as:

$$\Delta Q(N_b) = \frac{1}{4\pi}\beta_0(s)\Delta k(s, N_b) \tag{4.4}$$

where equation (4.4) is valid in the limit of a small tune shift and small quadrupolar error. Quantitatively one can compute these limits taking the correct beta beating formula and the approximated one obtained inverting equation (4.4).Taking the ratio one gets a solution shown in Figure 4.1 for different tunes [23]. Having in SPS $Q_x = 26.13$ and $Q_y = 26.18$, we can accept a total tune shift around $\Delta Q_{max} = 0.05$ that corresponds to a single max quadrupolar error equal to $\Delta k_{max} \simeq 0.01$.

In this approximation, multiple quadrupolar errors can be treated via superposition of effects, simply summing all the ΔQ_{k_j} due by the generic j^{th} quadrupole:

$$\Delta Q(N_b) = \sum_{j=0}^{N_{kicks}} \Delta Q_j = \sum_{j=0}^{N_{kicks}} \frac{1}{4\pi}\beta_0(s_j)\Delta k_j(s_j, N_b) \tag{4.5}$$

Since we work in the hypothesis of linear tune shift with intensity, from equation (4.5) follows that also quadrupolar strength must vary linearly with intensity:

$$\Delta k_j(s_j, N_b) = N_b \frac{\Delta k_j(s_j)}{\Delta N_b} \tag{4.6}$$

having $\Delta k_j(s_j, N_b = 0) = 0$. If we ignore coupling impedances between different elements in SPS, we can also decompose the total impedance Z_{eff} summing contributions from local positions:

$$\Delta Q(N_b) \propto \sum_{j=0}^{N_{imps}} Im(Z_{eff_j}) N_b \tag{4.7}$$

Since we get:

$$N_b Im(Z_{eff_j}) \propto \Delta Q(N_b)_j = \frac{1}{4\pi} \beta_0(s_j) \Delta k_j(s_j, N_b) \tag{4.8}$$

taking the derivative respect to the intensity N_b we have:

$$Im(Z_{eff_j}) \propto \frac{\Delta Q_j}{\Delta N_b} = \frac{1}{4\pi} \beta_0(s_j) \frac{\Delta k_j(s)}{\Delta N_b} \tag{4.9}$$

We can consider, finally, an impedance like a local *kick* acting exactly as an intensity dependent quadrupole. This will be the starting point to localize impedances.

4.2 SPS impedance

Sacherer's formula can be used to have a global estimation of the impedance in accelerators. In Figure 4.2 we have examples of impedance measurements for different years, starting from 2000.

Since the slope is directly proportional to the imaginary part of effective impedance, we can see that, from 2000 to 2001 a consistent impedance reduction is revealed, consequence of the impedance reduction program which took place from 1999 to 2001. In 2003, 5 new kickers were installed, and 4 more in 2006 as one can deduce by slope increasing. In 2007 one MKE kicker was removed and one fully shielded reducing the global impedance. The value one obtains is given, ideally, by the summation of all impedance sources ' contribution: in 2006, for example, total measured impedance was $23.6 M\Omega/m$ but kickers ' contribution was, from theory,only $8.7 M\Omega/m$ [21] [22].

Still 40% is missing: it can be reduced either, detecting new impedance sources to be quantified and "cured", or improving our understanding in impedance analytical models for every element. This thesis works in the former direction.

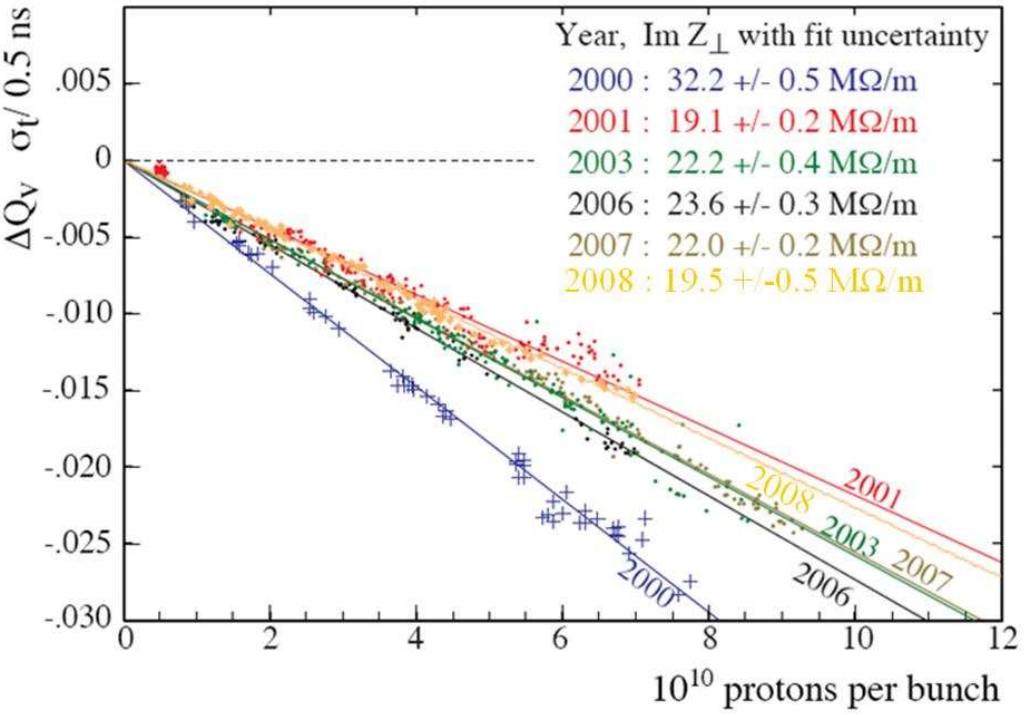

Figure 4.2: SPS vertical tune shift versus intensity from 2000 to 2008 (Courtesy of H.Burkhardt, B.Salvant)

4.3 Reconstruction algorithm

From equation (4.9) we obtained a link between local impedance sources and local quadrupolar strength errors. In order to reconstruct an impedance, then, we need to find a set of quadrupoles in the machine that could have the same effect as the impedances. Looking to the *phase advance beating* can be a solution.

4.3.1 Phase beating

A single quadrupole error induces a *beta beating* that, under the hypothesis given in Section 4.1, can be expressed with:

$$\frac{\Delta\beta(s)}{\beta_0} = -\frac{\beta_0(s_k)}{2sin(2\pi Q_0)} cos[2|\Phi(s) - \Phi(s_k)| - 2\pi Q_0]\Delta k L \tag{4.10}$$

where $\beta(s)$ and $\Phi(s)$ are respectively beta function and phase at the s location in the ring, "0" subscript refers to unperturbed quantities, "k" to the perturbed ones, Δk is the local kick given by a L length quadrupole in s_k position [10]. To compute phase advance beating in a generic s location we have to solve:

$$\Phi(s) = \int_0^s \frac{1}{\beta(\tau)}\, d\tau + \Phi(0) \tag{4.11}$$

Setting the initial phase $\Phi(0) = 0$ and developing β function at first order we get [10]:

$$\begin{aligned}\Phi(s) &= \int_0^s \frac{1}{\beta_0(\tau)\left(1+\frac{\Delta\beta}{\beta_0(\tau)}\right)}\,d\tau = \\ &= \int_0^s \frac{1}{\beta_0(\tau)}\,d\tau - \int_0^s \frac{\Delta\beta(\tau)}{\beta_0^2(\tau)}\,d\tau = \\ &= \Phi_0(s) + \Delta\Phi(s)\end{aligned} \tag{4.12}$$

Inserting (4.10) in (4.12) we obtain:

$$\begin{aligned}\Delta\Phi(s) &= + \int_0^s \frac{\beta_0(s_k)\Delta k L}{2sin(2\pi Q_0)}\frac{1}{\beta_0(\tau)}cos[2|\Phi(\tau)-\Phi(_k)| - 2\pi Q_0]\,d\tau = \\ &= \frac{\beta_k \Delta k L}{4sin(2\pi Q_0)}\int_0^s \left\{2\dot{\Phi}(\tau)cos[2|\Phi(\tau)-\Phi(s_k)|]cos(2\pi Q_0)\,d\tau\right\} + \\ &+ \frac{\beta_k \Delta k L}{4sin(2\pi Q_0)}\int_0^s \left\{2\dot{\Phi}(\tau)sin[2|\Phi(\tau)-\Phi(s_k)|]sin(2\pi Q_0)\right\}\,d\tau = \qquad (4.13)\\ &= C(s) + S(s) \qquad (4.14)\end{aligned}$$

Naming (C) the cosine part of the integral and (S) the sine one, we can develop separately the equation for cases $\Phi(s) > \Phi(s_k)$ and $\Phi(s) < \Phi(s_k)$.

When $\Phi(s) > \Phi(s_k)$ for the (C) part we obtain:

$$(C) = \frac{\beta_k \Delta k}{2sin(2\pi Q_0)}cos(2\pi Q_0)sin(\Phi(s))cos[\Phi(s) - 2\Phi(s_k)] \tag{4.15}$$

For the sine part, calculations are more involved since we have to split the integration:

$$\begin{aligned}(S) &= \frac{\beta_k \Delta k L}{4}\int_0^s 2\dot{\Phi}(\tau)sin[2|\Phi(\tau)-\Phi(\tau_k)|]\,d\tau = \\ &= \frac{\beta_k \Delta k L}{4}\left\{-\int_0^{s_k} 2\dot{\Phi}(\tau)sin[2(\Phi(\tau)-\Phi(\tau_k))]\,d\tau + \int_{s_k}^s \dot{\Phi}(\tau)sin[2(\Phi(\tau)-\Phi(\tau_k))]\,d\tau\right\} = \\ &= \cdots = \frac{\beta_k \Delta k L}{4}\left[2 - cos(2\Phi(s_k)) - cos(2(\Phi(s)-\Phi(s_k))\right] = \\ &= \frac{\beta_k \Delta k L}{2} - \frac{\beta_k \Delta k L}{2}cos(\Phi(s))cos[2\Phi(s_k) - \Phi(s)] \qquad (4.16)\end{aligned}$$

Summing (4.15) and (4.16) one gets:

$$\Delta\Phi(s) = \frac{\beta_k \Delta k L}{2} + \frac{\beta_k \Delta k L}{2sin(2\pi Q_0)}cos[2\Phi(s_k) - \Phi(s)]sin[\Phi(s) - 2\pi Q_0] \tag{4.17}$$

For $\Phi(s) < \Phi(s_k)$, following the same procedure as before, we can compute separately (C) and (S) contributions obtaining:

$$\Delta\Phi(s) = \frac{\beta_k \Delta k L}{2sin(2\pi Q_0)}sin(\Phi(s_k))cos[\Phi(s) - 2\Phi(s_k) + 2\pi Q_0] \tag{4.18}$$

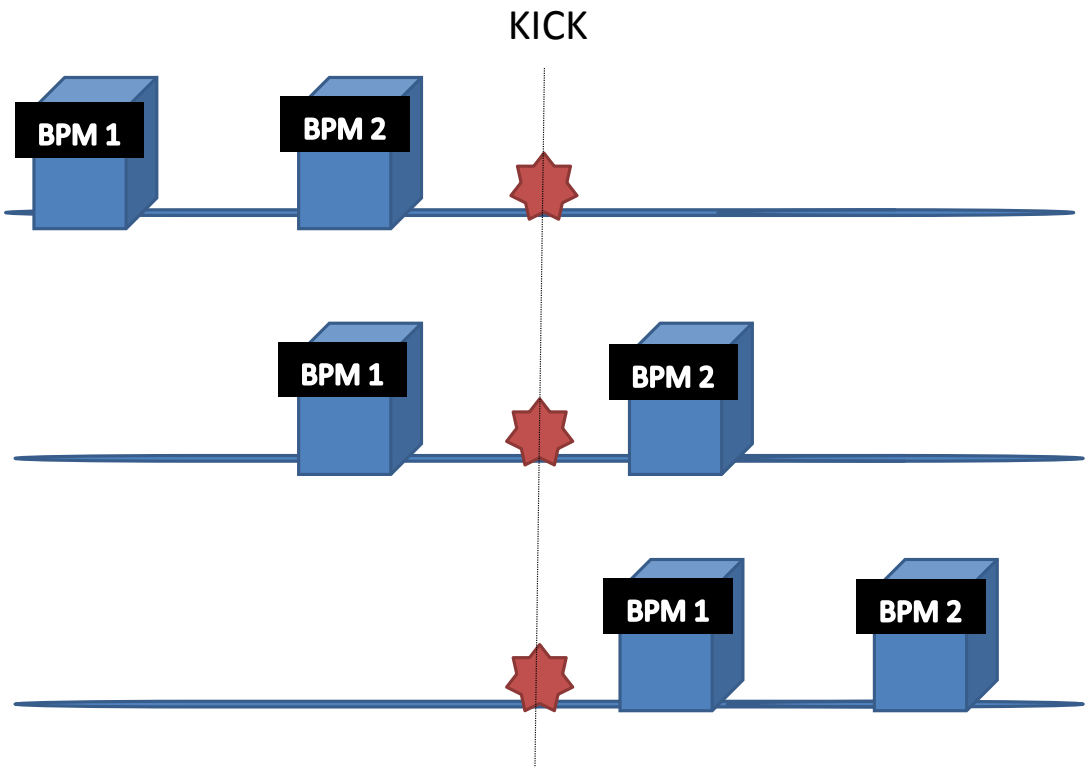

Figure 4.3: Three different cases to be considered in phase advance beating calculations.

4.3.2 Phase advance beating

As we will see in the following section, it is necessary to implement a different formalization of the problem, computing the phase advance beating between BPMs in place of the simpler phase beating (referred to any place in the accelerator circumference).

From equations (4.17) and (4.18) we have a relationship between local quadrupolar perturbation and phase beating that takes into account the relative position between kick and BPMs. Taken two generic BPM_1 at $s = s_1$ and BPM_2 at $s = s_2$, where s is the longitudinal position in the ring, placed a kick at $s = s_k$, we have three different cases as in Figure 4.3. For each of them we can compute the phase

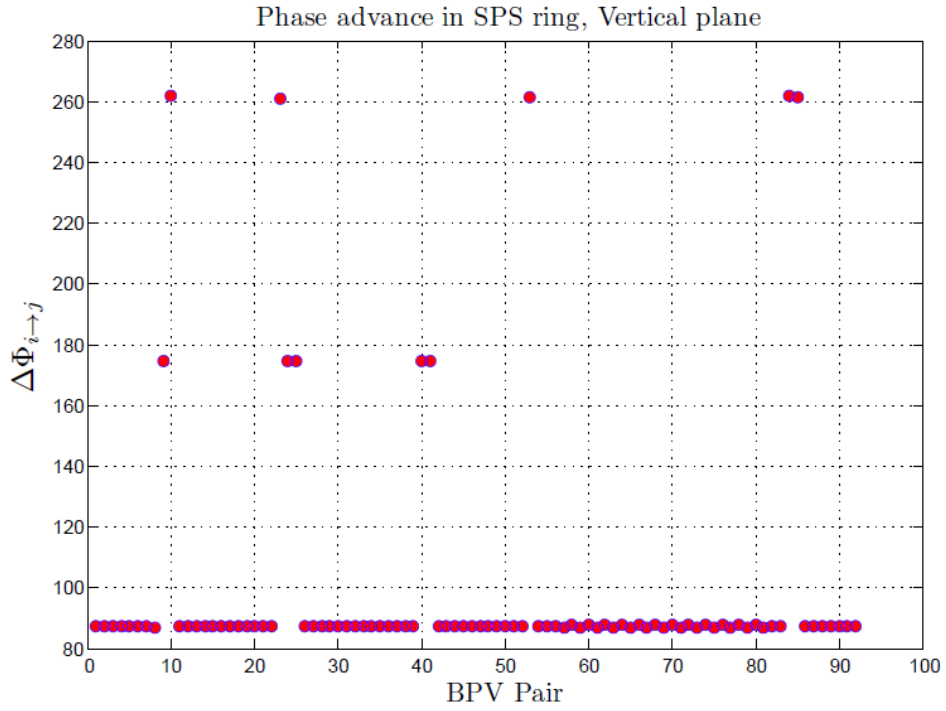

Figure 4.4: SPS phase advance between consecutive vertical beam position monitors BPVs

advance obtaining the following results:

$$\Delta\Phi(s_{1,2<k}) = \frac{\beta_k \Delta k L}{2sin(2\pi Q_0)}(cos(2\Phi_k - \Phi_2)sin(\Phi_2 - 2\pi Q_0) - cos(2\Phi_k - \Phi_1)sin(\Phi_1 - 2\pi Q_0)) \tag{4.19}$$

$$\Delta\Phi(s_{1<k<2}) = \frac{\beta_k \Delta k L}{2sin(2\pi Q_0)}(cos(2\Phi_k - \Phi_2)sin(\Phi_2 - 2\pi Q_0) - sin(\Phi_1)cos(\Phi_1 - 2\Phi_k + 2\pi Q_0)) \tag{4.20}$$

$$+ \frac{\beta_k \Delta k L}{2}$$

$$\Delta\Phi(s_{k<1,2}) = \frac{\beta_k \Delta k L}{2sin(2\pi Q_0)}(sin(\Phi_2)cos(\Phi_2 - 2\Phi_k + 2\pi Q_0) - sin(\Phi_1)cos(\Phi_1 - 2\Phi_k + 2\pi Q_0)) \tag{4.21}$$

In the SPS ring the relative distance between BPMs is shown in Figure 4.4. As one can see phase advance is quite always near 90° with some jump close to 180° and 270°. We can then specify (4.19), (4.20), (4.21) to these values.

If $\Delta\Phi(s_{1\to 2}) = n\frac{\pi}{2}$:

$$\Delta\Phi(s_{1,2<k}) = -\frac{\beta_k \Delta k L}{2sin(2\pi Q_0)} sin(2\Delta\Phi_{k\to 1} + 2\pi Q_0) \tag{4.22}$$

$$\Delta\Phi(s_{1<k<2}) = \frac{\beta_k \Delta k L}{2} \left[(cot(2\pi Q_0) sin(2\Delta\Phi_{k\to 1}) + 1\right] \tag{4.23}$$

$$\Delta\Phi(s_{k<1,2}) = \frac{\beta_k \Delta k L}{2sin(2\pi Q_0)} sin(2\Delta\Phi_{k\to 1} + 2\pi Q_0) \tag{4.24}$$

If $\Delta\Phi(s_{1\to 2}) = n\pi$:

$$\Delta\Phi(s_{1,2<k}) = 0 \tag{4.25}$$

$$\Delta\Phi(s_{1<k<2}) = -\frac{\beta_k \Delta k L}{2} cos(2\Delta\Phi_{k\to 1}) + \frac{\beta_k \Delta k L}{2} \tag{4.26}$$

$$\Delta\Phi(s_{k<1,2}) = 0 \tag{4.27}$$

Note that in equation (4.26) if $\Delta\Phi_{k\to 1} = \pi/2$ (i.e. the kick is in the middle of two 180° spaced BPMs) we get $\Delta\Phi(s_{1<k<2}) = \beta_k \Delta k L$, if $\Delta\Phi_{k\to 1} = 0$ (i.e. the kick is near the first BPM) we get $\Delta\Phi(s_{1<k<2}) = 0$.

4.3.3 Response matrix

Since we cannot measure phase beating for each point in accelerators but only using beam position monitors (BPMs), and there is a finite number of quadrupoles distributed in the ring, we have implemented a "discretized" form of our equations computing equations (4.19), (4.20), (4.21). Considering the phase advance beating between BPMs in a vector notation we have:

$$\begin{bmatrix} \vdots \\ \Delta\mu_{i,j} \\ \vdots \end{bmatrix} = \big[R\big] \begin{bmatrix} \vdots \\ \Delta k_q \\ \vdots \end{bmatrix} \tag{4.28}$$

where $\Delta\mu_{i,j}$ is the phase advance beating vector between positions i and j with $i, j \in (1, \ldots, N_{bpm})$ and Δk_q is the strength error versus intensity for each quadrupole in the ring with $q \in (1, \ldots, N_{quad})$, $[R]$ is the *response* matrix of our system. The response matrix has dimension $N_{bpm} - 1 \times N_{quad}$ and can be computed "switching on" quadrupoles one by one and calculating the phase advance response:

$$\begin{bmatrix} | \\ R_j \\ | \end{bmatrix} = \begin{bmatrix} 0 & | & 0 \\ \vdots & R_j & \vdots \\ 0 & | & 0 \end{bmatrix} \begin{bmatrix} 0 \\ \vdots \\ \Delta k_j = 1 \\ \vdots \\ 0 \end{bmatrix} \tag{4.29}$$

The system response is the phase advance beating due to the j^{th} quadrupole perturbation. It can be computed either analytically, with equations derived in the previous section, or using a lattice design tool like *MAD-X* [30]. In Figure 4.5 is shown the response matrix construction algorithm with *MAD-X*: perturbing j^{th}

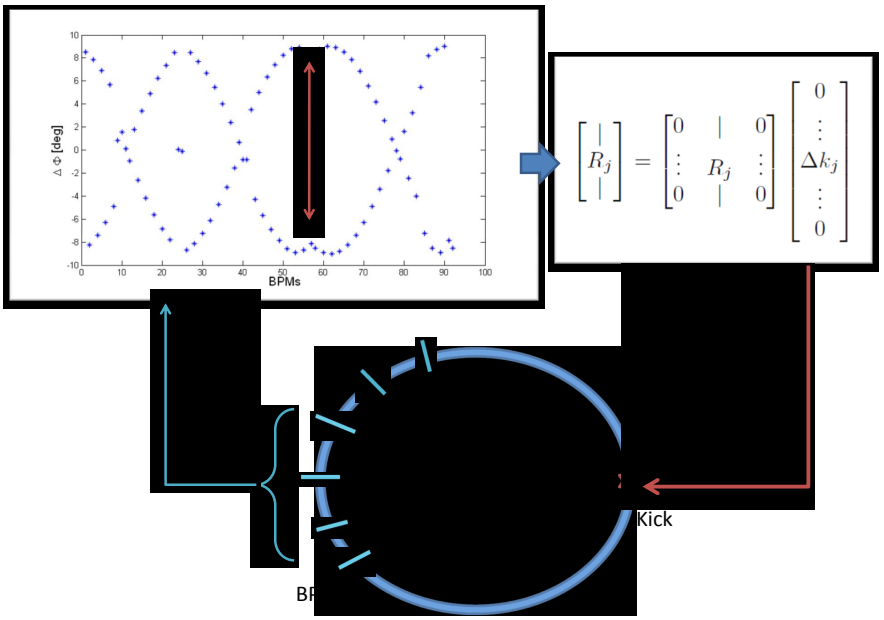

Figure 4.5: Response matrix construction algorithm.

quadrupole in the ring, the phase beating pattern presents a *kick* in its shape, this pattern is saved as j^{th} column in the response matrix.

Given, now, a certain phase advance pattern computed, for example, from a tracking program, we can invert the response matrix to get the vector of quadrupole strength that creates such pattern. Often, the R matrix is not a square matrix, and we have to solve the problem via Singular Value Decomposition (SVD) [24] [25]. the vector of quadrupole strength will be the *best fit* solution for the given phase advance pattern.

One last observation can complete the analysis started in Section 4.1. Increasing intensity we expect from equation (4.6) a linear growth in quadrupolar equivalent strength. A similar behaviour has to be expected from phase advance in any BPM pair since equations (4.19), (4.20), (4.21) are linearly dependent from Δk. The response matrix then, has to be the same:

$$\begin{bmatrix} \vdots \\ \Delta\mu_{i,j} \\ \vdots \end{bmatrix} = [R] \begin{bmatrix} \vdots \\ \Delta k_q \\ \vdots \end{bmatrix} \rightarrow \begin{bmatrix} \vdots \\ \frac{\Delta\mu_{i,j}}{\Delta N_b} \\ \vdots \end{bmatrix} = [R] \begin{bmatrix} \vdots \\ \frac{\Delta k_q}{\Delta N_b} \\ \vdots \end{bmatrix} \tag{4.30}$$

We can, in the end, invert via SVD the response matrix to derive $\frac{\Delta k_j(s)}{\Delta N_b}$ and use equation (4.9) to get the value of the local impedance.

4.4 Codes

Before presenting the complete reconstructing algorithm, we introduce here a series of codes we will use in the following, either for simulations, or for reconstructions.

4.4.1 *HEADTAIL*

Headtail is a tracking simulator code developed by G.Rumolo and F.Zimmermann [26] [27] and improved by D.Quatraro et al. [28] [29]. The original code version was able to simulate electron cloud and single wake field interactions, currently it is able to simulate multi interaction points given either by electron cloud, SC or wake fields, placed in any ring's position.

The code generates an initial transverse and longitudinal distribution (typically gaussian) placing a number of macroparticles N_{pr} that can be specified in the `hdtl.c` source code. The distribution is then transported between lattice elements using a *MAD-X* imported lattice `machinelattice.dat` previously matched at the horizontal and vertical tunes specified in the *HEADTAIL* config-file `test.cfg`.

In A is reported an example of config-file. In the following we briefly explain some parameter frequently used in our simulation:

`Switch_for_lattice_model_(0->simplified_1->from_MAD)`: this parameter (fixed to 1) avails us to select the *MAD-X* lattice to perform tracking between SPS elements.

`Number_of_particles_per_bunch`: this parameter $npr_0 inthecode$ fixes the number of particles the code is going to simulate. This value is used in numerically implemented analytical formulae describing SC and wake field interaction. The number of particles we are going to track (NPR in the code), instead, is fixed to 500000.

`Number_of_laps`: this parameter fixes the number of laps we are going to track. It is set to 512 turns by default as in measurements.

`Horizontal(Vertical)_tune`: these parameters set the horizontal(vertical) tune. It will be used in the *matching* routine in *MAD-X*. For SPS we set $Q_x = 26.13$ and $Q_y = 26.18$.

`x(y)-kick_amplitude_at_t=0_[m]`: this parameter displaces the centroid from the reference center $(x, y) = (0, 0)$. It is set to 0.001m.

`Switch_for_wake_fields`: this switch avails us to simulate wake field interaction with bunch. Every other effect like electron cloud and SC, is not taken in account.

`Switch_for_pipe_geometry_(0->round_1->flat)`: this parameter avails us to chose the way the wake field is going to interact with every particle in the bunch. In our simulations it is set to 9 and implements the dipolar and quadrupolar interaction we introduced in 3. Formula (3.56) is implemented numerically in the code as:

$$\Delta\dot{y}_i(s_j) = \sum_{j<m}^{N_{bin}} q^2 \frac{N_j}{\beta^2 E}(W_{dip}(\Delta)\bar{y}_s + W_{quad}(\Delta)y_i) \tag{4.31}$$

where Δ is the distance between particle and centroid. Dividing the bunch in N_{bin} slices, we can sum contribution of quadrupolar and dipolar wakes from each slice in front of the test particle: for quadrupolar, we compute equation (4.31)

for each particle in the test slice, for dipolar, we refer to the source displacement given by $\bar{y}_s$ the average displacement of the source slice.

Before the tracking, *HEADTAIL* initializes the particle phase-space distribution using `init_values()` function, charges all the elements wakes in dedicated tables, then the machine is divided in lattice elements calling `GetTwiss.c`, a *C* code used to manage the lattice produced by *MAD-X*. The distribution is transported via lattice matrix multiplication element by element for the specified number of turn. For every element, *HEADTAIL* "looks" to a reference file called `ELEMENTS_NAMES.txt` where the beginning, ending of SPS, wake field interaction points (IP) and BPMs are identified by a common flag):

BPM In case a BPM is detected, the code simply dumps centroid parameters like $\bar{x}$, $\bar{x}'$, $\bar{y}$, $\bar{y}'$, $\bar{z}$, $\bar{z}'$ in a file. Note that these parameters are referred to the centroid position only, an average over all the tracked particles is previously performed.

IP In case an interaction point is detected, the bunch is sliced in N_{bin} slices and using equation (4.31), a transverse kick is calculated for each particle. At the end the average kick over all the particles is computed and added to the centroid angles $\bar{x}'$ and $\bar{y}'$.

END In case the end of the machine is detected, the centroid positions and angles are transported to the starting element and a new turn is executed until the last one is reached.

In our simulation we used wakes from kickers computed using Yokoya factors in equation (3.115). These are contained in files where dipolar and quadrupolar, horizontal and vertical components, are ready to be used (i.e. `MKE.41634.Ydip` refers to the vertical dipolar component in the `MKE.41631` kicker).

Kickers are classified in 4 families referring to their use: MKEs, used to extract the beam from SPS, MKQs, used to perform tune measurements, MKDs, used to dump the beam, MKPs, used for injection. In Appendix B we report their wakes.

The *HEADTAIL* release we used is able to compute impedances effects by specifying the element name in which the impedance is located ad tracking particles for the specified number of turns. Here follows an example of command used to launch *HEADTAIL* simulations:

```
./hdtl latticemodel.dax START 3 BPV MKE
```

where `latticemodel.dax` is the *MAD-X* file will create the SPS lattice, `START` sets the SPS beginning to the first element of the lattice, `3` is a flag to specify to the `GetTwiss.c` code that we are going to record *MAD-X* functions in every element, `BPV` specifies we are going to dump datas in every horizontal beam position monitor (using simply `BP` we select also vertical ones), `MKE` selects IPs in every extraction kicker.

4.4.2 *MAD-X*

MAD-X is a lattice development tool commonly used at CERN to study optics in accelerators. In our work it will be used to construct the response matrix for the

SPS 2008 model. It is possible, in particular, to compute the twiss functions α, β, μ for both horizontal and vertical planes, to match the lattice for a given tune $Q_{x,y}$ in both planes acting on quadrupolar strength, to install new elements in the lattice sequence. A complete *MAD-X* features description can be found in [30].

4.4.3 *SUSSIX*

SUSSIX is a signal analysis tool developed by R.Bartolini and F.Schmidt [31] [32] able to find harmonics in betatron motion. It implements a particular *FFT* algorithm either on real or complex signals. We will use it to process *HEADTAIL* tracking files in order to get parameters like betatron tune and phase measured at every BPM position in the ring. The number of turns we processed is 512. The maximum accuracy we can get for the tune is $\sigma_Q \simeq 10^{-7}$. The typical curve of phase accuracy with number of turns is shown in Figure 4.6. We can observe, for 512 turns, a $\sigma_\phi \simeq 10^{-3}$.

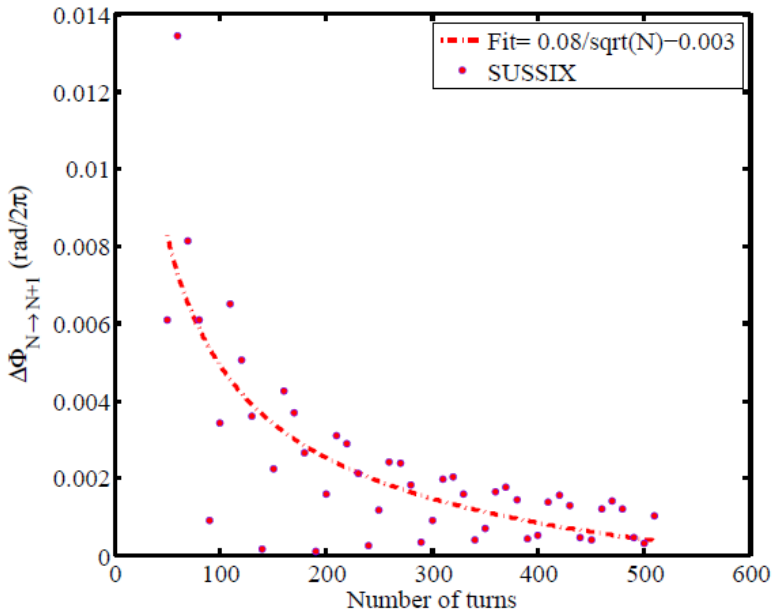

Figure 4.6: Fit of phase accuracy with number of turns.

4.4.4 Simulation system

The reconstructing algorithm is represented in Figure 4.7. One can "insert" in the SPS model tracked by *HEADTAIL* wake fields corresponding to different elements. In our simulation we used mainly kickers modeled with Yokoya or Tsutsui computed wake fields. Once the impedances are located, many simulation at different bunch population are performed and tracking data from all BPVs and BPHs are collected in different files. This analysis will be, hopefully, substituted by real measured data if this algorithm is found to be enough robust. A Fourier analysis is then performed using *SUSSIX* toolbox in order to get values of phase advance between BPMs for each intensity. These values are then collected in a vector ordered by corresponding

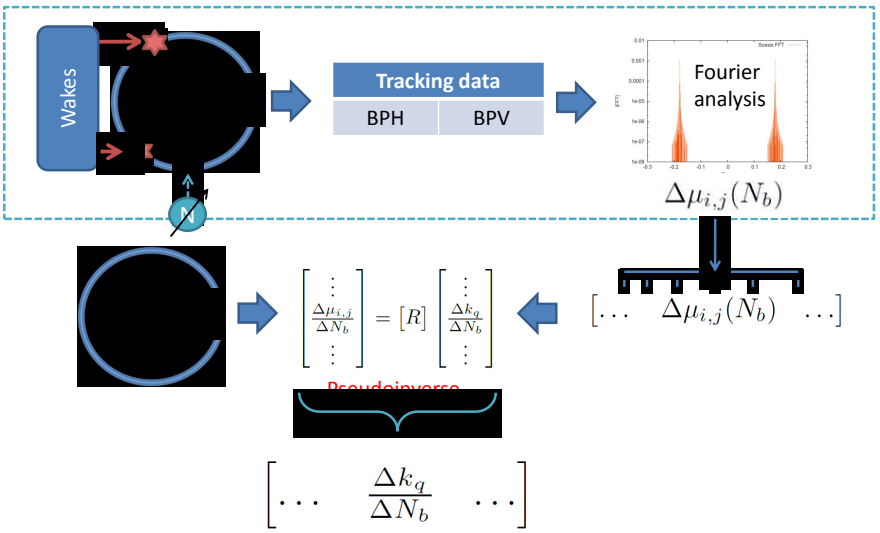

Figure 4.7: Recostruction algorithm.

intensity. At this point it is possible to use the same response matrix presented in Section 4.3.3 since phase advance and equivalent kicks are supposed to be linearly intensity dependent. The inversion is a *pseudo-inversion* since the response matrix is rectangular, then, our solution will be in a least square sense, the best solution.

Here we conclude the detection algorithm theoretical foundation. In the next Chapter we will present some old result performed by R.Calaga, G.Arduini and D.Quadraro, and a series of new simulations and corrections to the algorithm.

Chapter 5

Algorithm upgrade and limits

In this chapter we will present some previous result from reconstructions and our present studies and issues around the case of one single impedance detection.

5.1 Past results

First impedance distribution measurements were performed in LEP by D.Brandt, P.Castro and others [33]. The original idea was to measure the accumulated phase advance (phase advance from the first BPM to the n^{th} one with $n = 2 \dots N_{BPM}$) and this made possible detecting cavities as the larger contributor to the global LEP impedance.

In the following years, the same algorithm was applied in the SPS by G.Arduini, C.Carli and F.Zimmermann [34]. The following work developed by R.Calaga and D.Quatraro [35], [36], enabled us to use the *HEADTAIL* code to simulate and detect impedance, building up a useful benchmark system.

First simulations were performed using only defocusing quadrupoles (108 elements), since, from theory, an impedance acts exactly like a defocusing quadrupole (at least for the vertical plane in the SPS). Kicker impedances with an average value of $0.5M/m$, were inserted in the lattice model as explained in Section 4.4.4. The same kind of simulation was performed using all quadrupoles (232 elements) available in SPS, increasing the freedom degrees and the size of response matrix. An example of these reconstructions can be found in Figure 5.1. As one can observe, reconstruction with all quadrupoles seems to be better than the same one using only defocusing quadrupoles. This can be understood since, in principle, impedances can be displaced everywhere in the ring, and not only in defocusing quadrupole positions. Increasing the number of fit elements, then, we can have "more chances" to detect correctly impedance sources. One can then think to insert as many quadrupoles as possible, but, as we will see in the following sections, this will insert degeneracies in the response matrix leading to a spread in reconstructed impedances.

5.2 Thin lenses insertions

Even if reconstructing with all quadrupoles gave better results in comparison with only defocusing ones, it is convenient to implement a different set of "reconstructors": thin lenses.

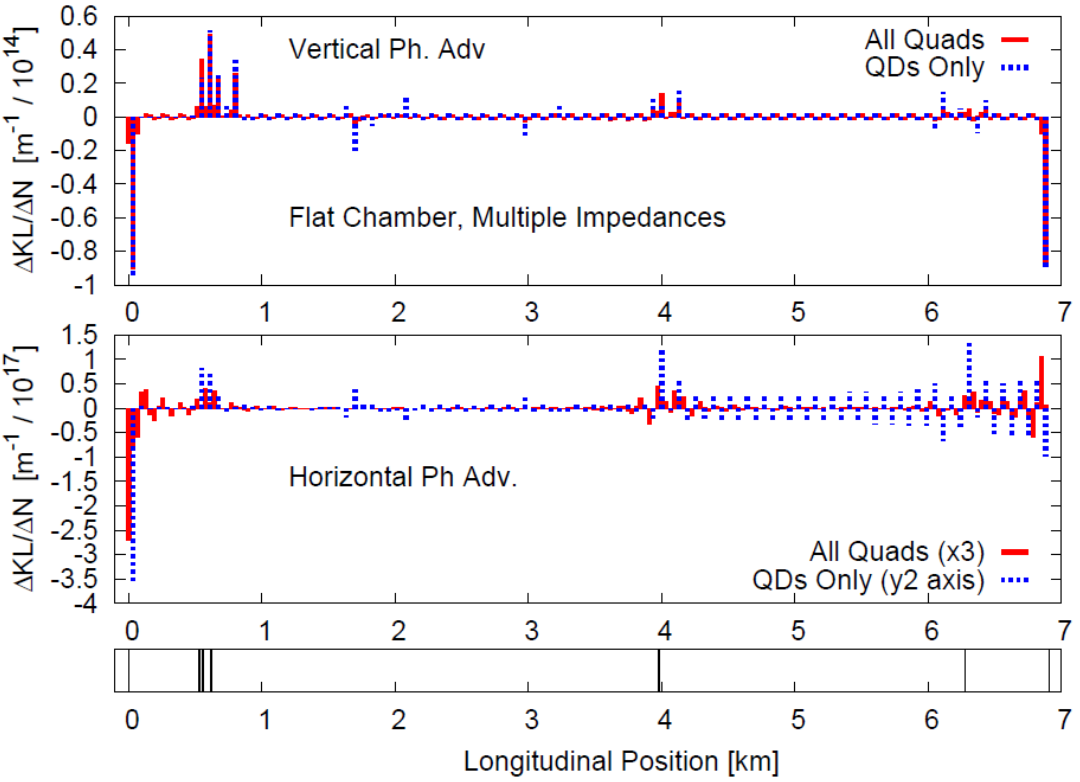

Figure 5.1: Example of impedance detections using only defocusing quadrupoles and all available quadrupoles in SPS. Positions of simulated impedance sources (SPS kickers) is shown in the bottom bar.

A thin lens is an ideal optic element that models a kick in particle's angle leaving unchanged particle position. Given z and z' generic position and angle in phase space, the transfer matrix for such kind of elements is given by [37], [10]:

$$\begin{bmatrix} z_2 \\ z_2' \end{bmatrix} = \begin{bmatrix} 1 & 0 \\ -\frac{1}{f} & 1 \end{bmatrix} \begin{bmatrix} z_1 \\ z_1' \end{bmatrix} \tag{5.1}$$

In case of a "thick" defocusing quadrupole, instead, we have:

$$\begin{bmatrix} z_2 \\ z_2' \end{bmatrix} = \begin{bmatrix} cosh(\sqrt{|K|}l) & \frac{1}{\sqrt{|K|}} sinh(\sqrt{|K|}l) \\ \sqrt{|K|} sinh(\sqrt{|K|}l) & cosh(\sqrt{|K|}l) \end{bmatrix} \begin{bmatrix} z_1 \\ z_1' \end{bmatrix} \tag{5.2}$$

Since an impedance is modeled with equation (4.31), a thin lens should be closer to the model.

In the following we will place a thin lens in front of every quadrupole element as shown in Figure 5.2. Since we developed analytical formulas for response matrix calculation, it will be also easy to insert thin lenses in other positions in the lattice without modifying the *MAD-X* configuration files. This avails us to benchmark impedance localization reconstruction: inserting lenses in front of the impedance element should let us achieve the best reconstruction as possible.

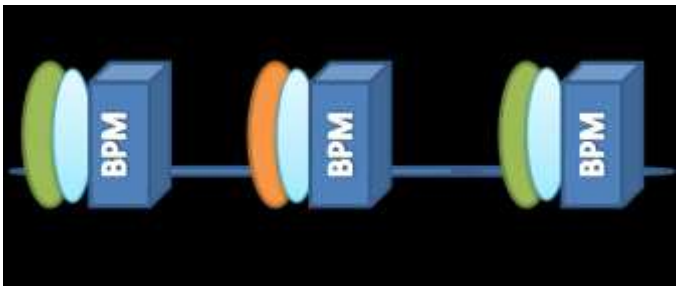

Figure 5.2: Lenses insertion. We inserted a thin lens element initially in front of each quadrupole.

5.3 Single kick reconstructions

The most simple case we can simulate to benchmark the algorithm, is taking a single impedance in SPS, or a group of elements very close to each other and trying to reconstruct the position. In a first set of simulations we left unchanged the lens positions, that were put in front of every quadrupole. In the following we also tried to change their position.

As presented in Section 4.4.1 kickers are the most important contributors to the SPS global impedance. For this reason we simulated separately the four kickers families, "switching on" their wake fields in the *HEADTAIL* wake field interaction module. In Appendix B we also reported the main twiss parameters for each kicker. After tracking particles for 512 turns in a range of intensity from $1.0{\cdot}10^{10}$ to $14.0{\cdot}10^{10}$ particles in a single bunch, we extracted phase values for each intensity and each

BPV or BPH using *SUSSIX* spectrum analyzer tool. After computing phase advance for each pair of BPMs, phase advances are collected in a vector function of intensity and a linear fit is computed to get the phase advance slope versus intensity. Using relation (4.28) we compute the pseudoinverse for the response matrix to get the equivalent quadrupolar error slope versus intensity.

The case for MKPs is presented in Figure 5.3 As one can observe the recon-

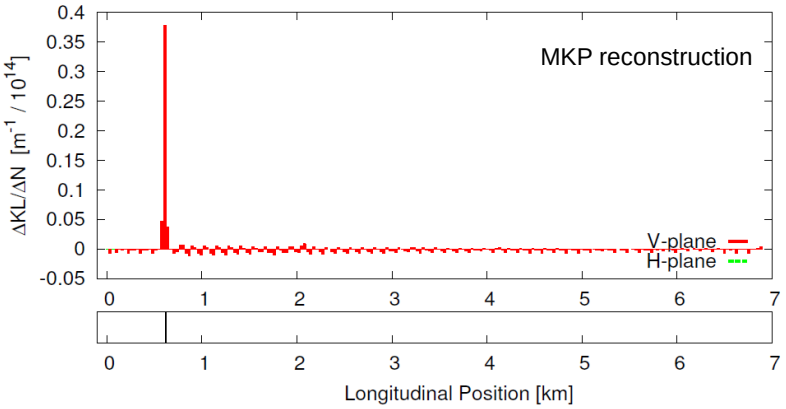

Figure 5.3: MKPs reconstruction using lenses in front of each quadrupole. MKPs position is shown in the bottom bar. Horizontal plane reconstruction is almost null compared with the vertical one since this impedances mainly affect vertical plane.

struction is quite good, but this is a particular case since MKPs are the strongest kicker source of impedances in SPS: as we will see in the following, the detection quality is strongly dependent from the impedance magnitude, the beta function in the kicker place and the numerical accuracy in phase computing. Figure 5.4 shows reconstruction examples for MKDs, MKEs and MKQs. It is interesting to notice the presence of peaks at the first and last lens used for reconstruction in both planes, and the presence of peak splitting for MKDs, MKQs, MKEs impedances. Part of this behaviour is correlated to the shape of the response matrix, and in particular to the position for the chosen set of lenses.

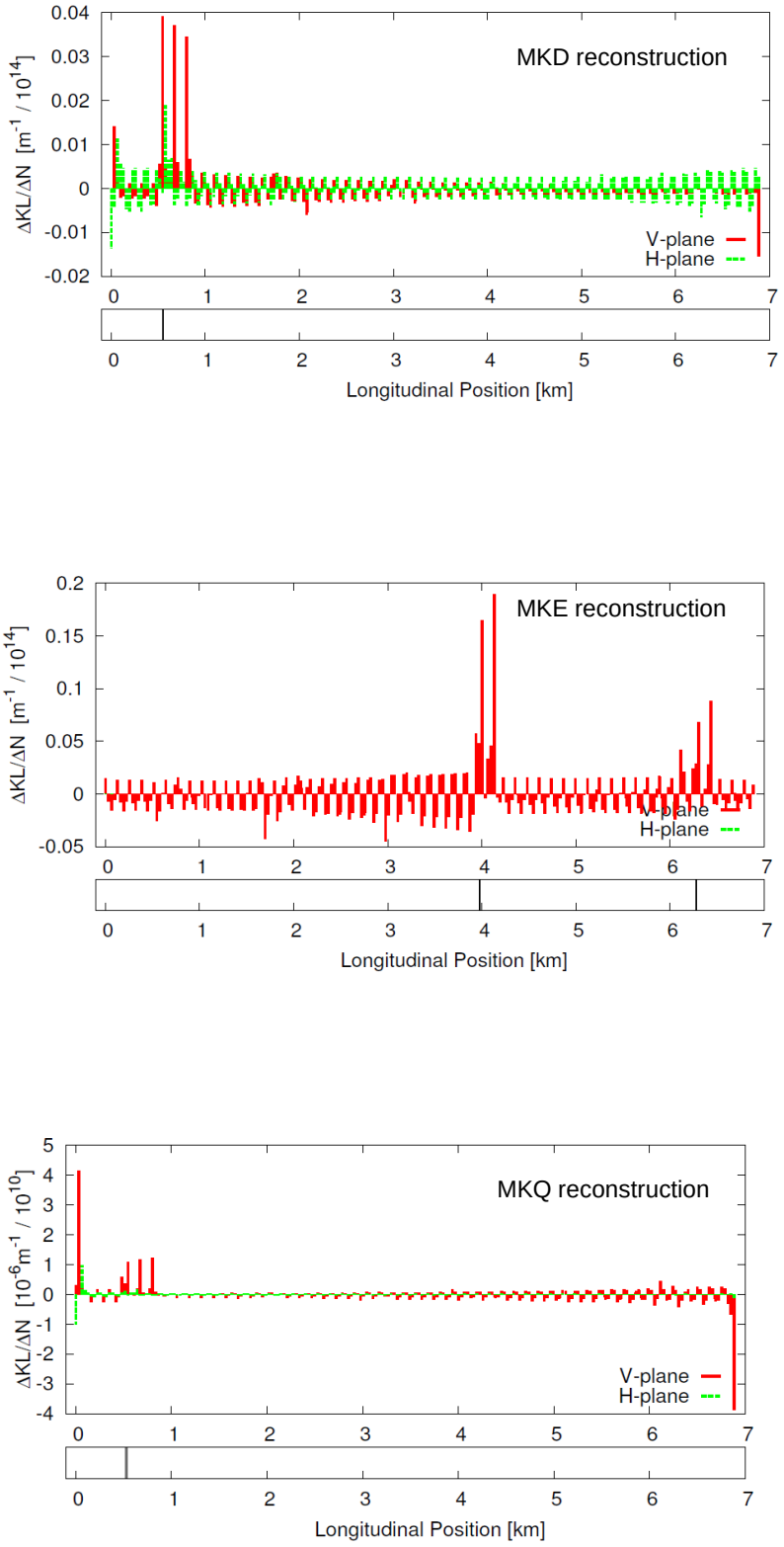

Figure 5.4: Different examples of reconstruction. From top to bottom: MKD, MKE, MKQ.

5.4 Response matrix studies

One way to analyze what is happening during the reconstruction is to visualize the response matrix in order to find particular behaviours that can lead to peak splitting phenomena. In order to reduce the response matrix computing time, we implemented in *MATLAB* equations (4.19), (4.20), (4.21) avoiding the computing time requested from the *MAD-X* scheme shown in Figure 4.5, and passing from 1.5 hours to few seconds time computing. This is possible for this particular kind of problem where a closed analytical formula could be derived.

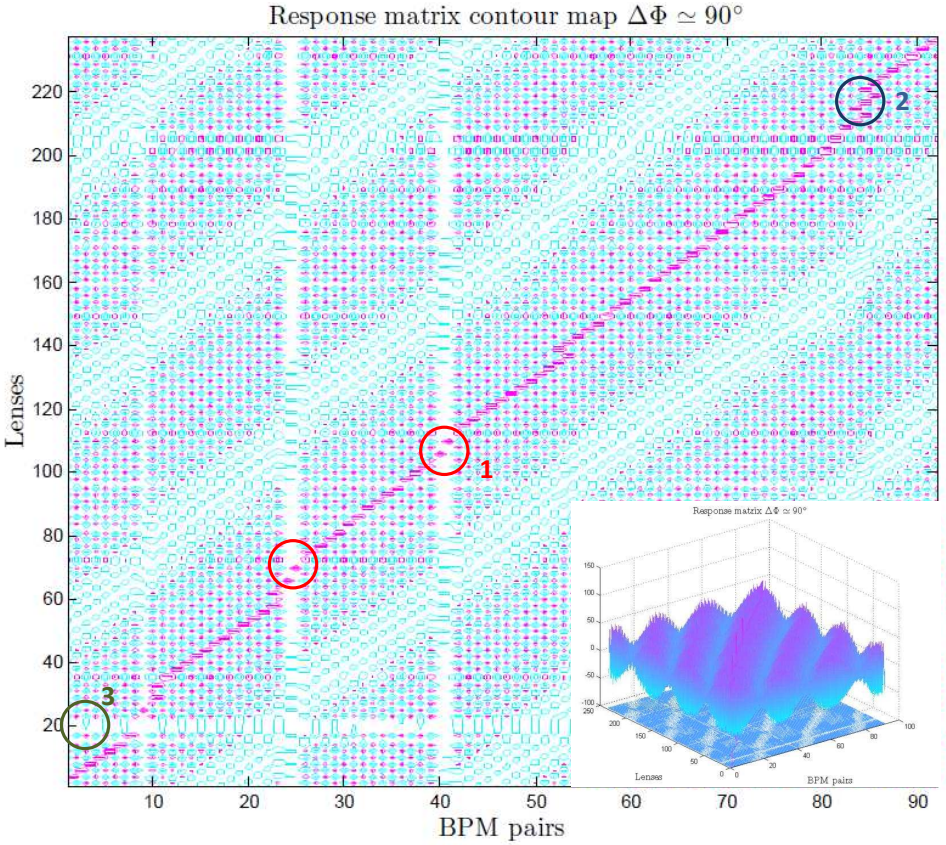

Figure 5.5: Response matrix contour plot. This matrix correspond to the one used in past simulations performed by G.Arduini, R.Calaga and D.Quatraro: thin lenses are simply placed in front of every quadrupole. In the horizontal plane BPMs are reported, in this case for the vertical plane, in the vertical axis is the recontruction lens position. Looking to rows one can see how a kick is "seen" by every BPM pair, looking to coloumnn how a BPM pair see a kick. Circles "1" refer to 180° phase advance BPM pairs, circles "2" refer to 270° phase advance ones, "3" refer to high density defocusing quadrupoles.

In Figure 5.5 we plotted the phase advance response for each kick given by thin lenses. The set of reconstructors is the same used in the past by G.Arduini, R.Calaga and D.Quatraro: thin lenses are simply placed in front of every quadrupole. In x-plane we have the number of BPMs (in this case BPVs), in y-plane the number of kick is reported. Reading rows in this "phase map" we observe the response seen by BPMs for a kick applied in the corresponding lens, reading the columns we recognize the phase beating seen for a certain pair of BPMs. A serie of further observations can be done:

1 Red circled points (number '1' in the picture) correspond to 180° phase jump in SPS lattice. These jumps, bigger respect to the 90° base FODO cell, are necessary to put elements like kickers. As we derived from equations (4.25), (4.26), (4.27), 180° spaced BPMs are going to see phase advance beating only in their between. Kicks applied outside these pairs are not revealed. This property is valid for any multiple of 180°. In SPS, one could think to implement a 180° lattice taking two series of BPMs, even and odd, in order to enhance this behavior, but nothing will change from the detection point of view, since we are applying a linear combination in response matrix's lines. Combining linearly response matrix lines, one can also implement the accumulated phase advance detection cited in section 5.1 about LEP impedance detections. Moreover plotting response matrix could help in checking the effect of noise in real data.

2 Blue circled points (number '2' in the picture) show duplication of lines. These points correspond to 270° phase advance in the SPS lattice. Unfortunately, when we have these kind of jumps, different kicks happening in between two 270° spaced BPMs creates identical phase advance beating patterns (same lines in the response matrix). This is a degeneration that cannot be avoided except if we delete some reconstructor (equivalent to delete lines from the response matrix).

3 The regularity one can observe in the response matrix is also caused by response with different magnitude: a kick given in the proximity of a defocusing quadrupole (with respect to the horizontal plane) will be reduced by short beta function in the vertical plane, vice versa near a focusing one, the response is enhanced.

4 The big blank space corresponding to the 20^{th} kick (20^{th} line in response matrix) is due to the presence of a group of quadrupoles placed at very short distance one from the other. The response, then, is similar, and having a low beta function, is almost null.

After these observations we tried to reduce the number of reconstructors in order to "diagonalize" as much as possible our response matrix[1]. We carefully analyzed the relative displacement of BPMs, quadrupoles and kickers. Following equations (4.22), (4.23), (4.24) for 90° and 270° phase advance jumps, and equations (4.25), (4.26), (4.27) for 180° phase advance jumps, to guarantee a good reconstruction we can choose quadrupoles in order to cover one period of beating oscillation. Since phase advance beating oscillates at double the tune value, in a generic FODO cell we will have 90° phase advance in each quadrupole. In Figure 5.6, we present our simple choice for lenses position: we put lenses near every focusing (F) or defocusing (D) quadrupole covering one oscillation period. Referring, still, to the vertical plane, in 90° phase advance pairs we put one thin lens near the first BPV, and one in the middle (corresponding to the defocusing quadrupole in the FODO lattice) (case (a) in the scheme). Analogous is for 180° and 270° phase advance pairs (case (b), (c)).

[1]One could think to take one quadrupole for each pair of BPMs in order to have a perfectly diagonal response matrix, but this will reduce the resolution in detection and will create strong peak splitting phenomena in case the impedance is not located near the reconstructor.

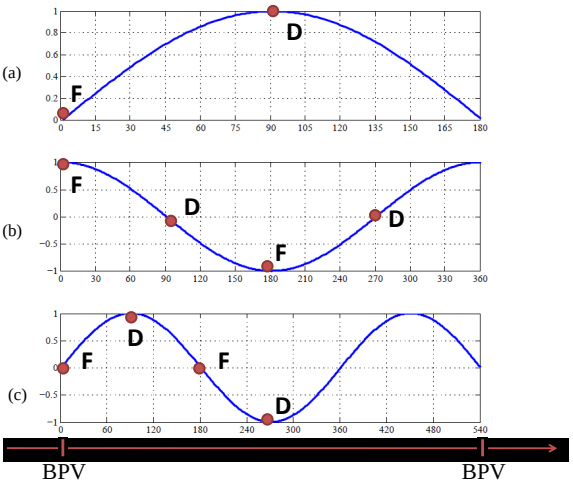

Figure 5.6: Scheme used for placing reconstructing lenses in SPS ring between two BPMs. Case (a), (b), (c) show in term of phase advance, the position we choose (red spot) and the corresponding optic element ('F' = Focusing quadrupole, 'D' = Defocusing quadrupole) between two BPVs. We avoided choosing points in which response is the same because this leads to line duplication in the response matrix.

Since we are reconstructing kickers impedances, placing lenses near quadrupoles will not give us a perfect detection since $\Delta\Phi_{k\to1}$, in the previous set of equations, is fixed by the position of lenses. In the future we will implement a "sliding lenses" scheme, iterating the reconstruction algorithm moving lenses position in order to fit better the position of impedance. At the moment we placed lenses near kickers because this should guarantee the best reconstruction as possible.

The final result is a more regular sequence of BPMs and lenses, with higher lenses density near kickers. An example is shown in Fig. 5.4 zooming SPS circumference between 350 and 750 meters. Blue circles represent lenses position, used for reconstruction, red circles, BPVs, and green diamonds, in the order, MKQs, MKDs, MKPs kickers. The picture is referred to the vertical plane, so we can recognize the typical phase spacing for a FODO cell (Focusing quadrupole - Optics - Defocusing quadrupole - Optics). Of course BPVs are placed in the proximity of focusing quadrupoles because, there, vertical beta function is higher and beam signal can be revealed better. We decided to put lenses exactly in kicker positions (overlapping of blue circles with green diamonds) in order to perform reconstruction in most ideal conditions. It can be noted, also, that the central BPV is missing in the following two FODO cells (FODOFODO). This make the measured phase advance between BPVs equal to $90+90 = 180$ degrees, with characteristics explained in Section 4.3.2. In every other position in SPS, the scheme of Figure 5.6 is instead applied.

5.4.1 Normalizing the response matrix

One more observation can be done. Since phase beating, from equations (4.22), (4.23), (4.24) and (4.25), (4.26), (4.27), is dependent in magnitude by the value of beta function in kick position, we can apply a normalization of the response matrix respect to the beta function. In this way we will obtain a smoother response matrix. Moreover, from equation (4.9), the imaginary part of impedance is proportional to

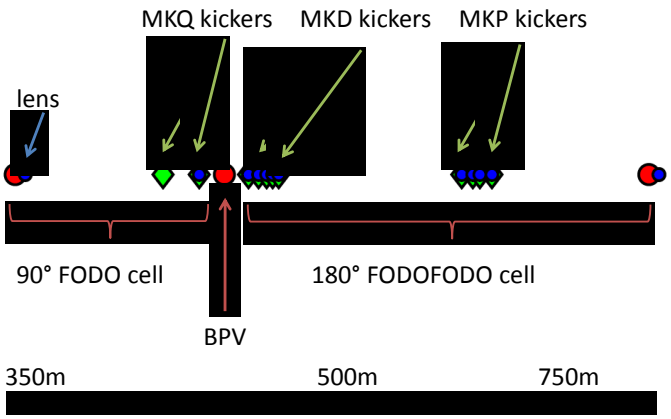

$FODO cell with MKQ kickers, and the 180^{\{circ}$ one with MKP and MKD kickers.

$\beta_k \Delta K / \Delta N_b$. Normalizing to the beta function we will automatically reconstruct this product. In Figure 5.8 we show two different reconstructions: the first one (case 'F') is obtained perturbing SPS lattice near a focusing quadrupole, the second one (case 'D'), perturbing near a defocusing one. As one can observe, the minimization algorithm tries to reconstruct our imposed kicks mainly using focusing quadrupoles since their response is higher in magnitude respect to the defocusing ones. In this way the norm for $[\dots, \Delta k_q, \dots]$ in equation (4.28) is kept at the minimum possible value and we see a split in peaks.

Normalizing the response matrix, we give the same weight to every quadrupole since we artificially put $\beta_k \Delta K / \Delta N_b = 1$ in the response matrix construction. In this way focusing and defocusing quadrupoles work at the same way as can be seen in Figure 5.9 where peak splitting has disappeared.

We implemented all these observations in order to comput e a new response matrix. This is shown in Figure 5.10. As one can observe, the duplication of lines near the 20^{th} lens (20^{th} line in response matrix), this time, is wanted, and it corresponds to lenses located near MKQs, MKDs, MKPs kicker positions as in Figure 5.4, the response is smoother because we normalized with beta function. Of course, we still see 90° and 180° jumps because number of used BPMs is always the same and cannot be increased, and kickers impedances are mostly placed in these locations.

5.5 Algorithm limits

During this work many simulations and detections were performed in order to study the reconstruction quality and define limits for the algorithm. We simulated reconstruction placing all the kickers, only MKDs or MKEs, MKPs, MKQs, or just one kicker from one of these 4 families. Many effects seem to play a role in a very different way as one can observe in Figure 5.4, where we tried to reconstruct MKE kickers: the kickers position is not clearly recognized, even if we put lenses also in kickers positions, and peaks at beginning and ending in the lattice start to appear. For this reason we have to fully understand how a single-kick reconstruction works.

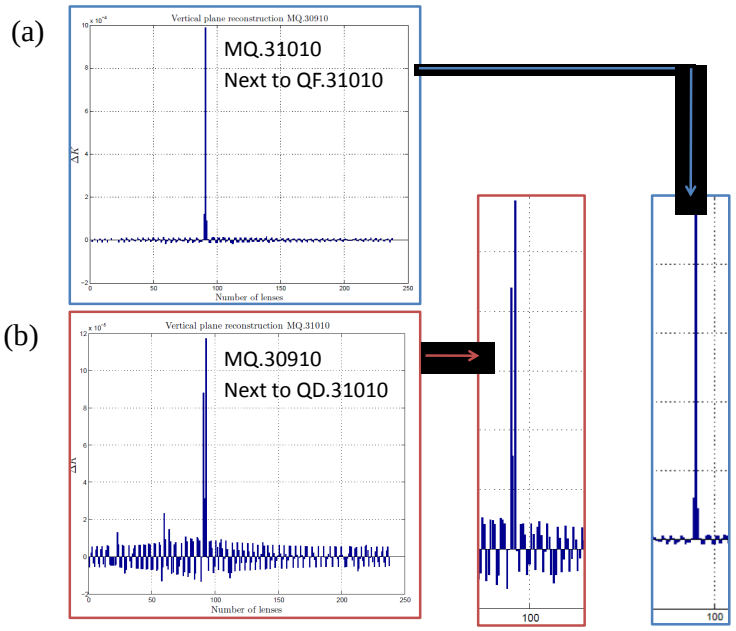

Figure 5.8: Example of peak splitting without response matrix normalization. A kick placed in a low beta position will be reconstructed mainly using two near focusing quadrupoles.

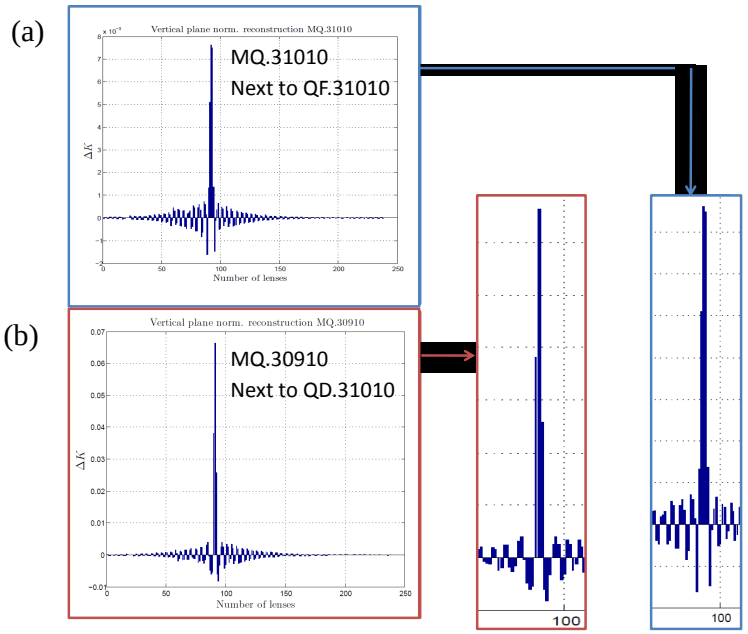

Figure 5.9: Example of peak splitting correction normalizing response matrix. Defocusing and focusing quadrupoles will have the same weight in the reconstruction.

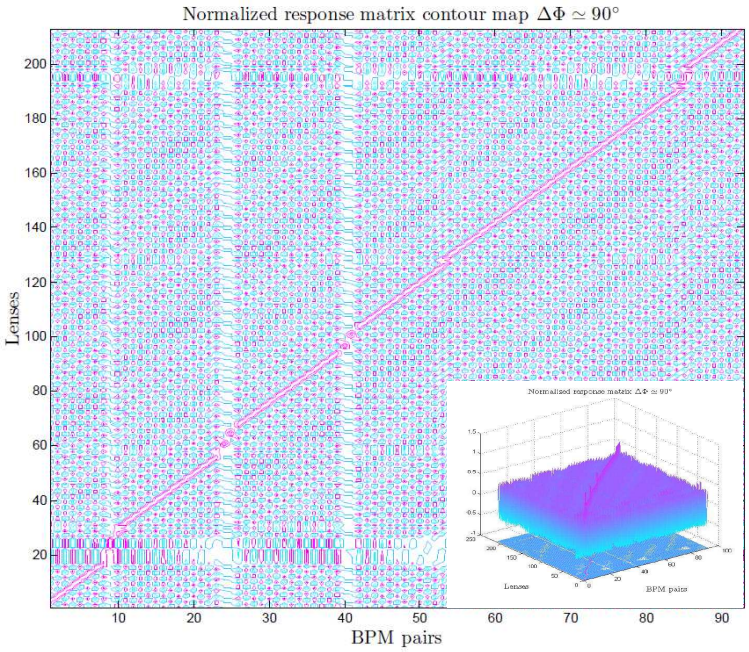

Figure 5.10: New response matrix. The diagonal is smoother respect to the previous case since we normalized with beta function. Lenses were put in kicker positions to guarantee the best reconstruction even if this lead to line duplication at least in these position

5.5.1 Accuracy and linearity limits for phase advance beating

The base assumption in the detection algorithm is written in equation (4.30): we have to define the range of validity in approximating the reconstruction matrix for the slope $\Delta\mu_{i,j}/\Delta N_b$, with the reconstruction matrix for phase advance beating $\Delta\mu_{i,j}$. This analysis can be done varying the strength value k_z in a lens for a certain range, following *MAD-X* model in Figure 4.5. Looking to the phase advance we simulate a quadrupolar strength variation with intensity. We have to use the non linear model content in *MAD-X* since the analytical equations we derived are a linear approximation.

Results from this simulation are shown in Figure 5.11 where we show *MAD-X* non linear response and linear approximation.

On the horizontal axis we reported in logarithmic scale the strength variation ΔK we changed in one lens near a focusing quadrupole (i.e. where beta function is maximum and the beating effect is enhanced). We divided the plot in three different sections:

1 Section 1 includes the range for $\Delta K = (10^{-5}, 10^{-4})$. In this range can be found a phase variation $\Delta\Phi \simeq 10^{-4}$, then, referring to Section 4.4.3, we are near the resolution for our spectrum analysis.

2 Section 2 includes the range for $\Delta K = (10^{-4}, 10^{-3})$. In this range can be found a phase variation $\Delta\Phi \simeq 10^{-3}$ and the non linear model is still close to the linear approximation in term of accuracy limit.

3 Section 3 includes the range for $\Delta K = (10^{-3}, 10^{-2})$. In this range can be found a phase variation $\Delta\Phi > 10^{-2}$ and the hypothesis of small tune shift given in

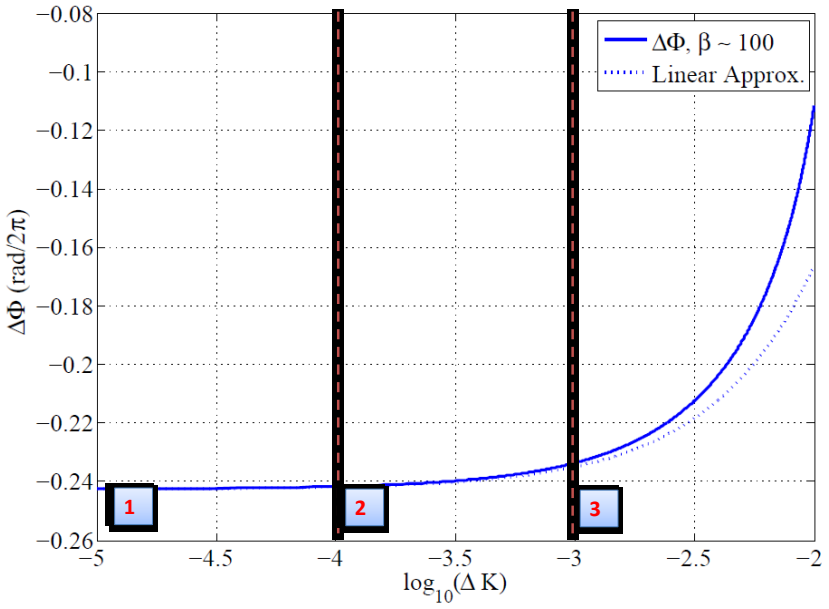

Figure 5.11: *MAD-X* phase advance beating non linear model, and linear approximation with response matrix. In x-plane is shown the *log*10 thin lens error ΔK, in y-plane the produced phase advance beating between two pair of BPMs.

equation (4.4) is no more valid having $\Delta Q \simeq \Delta K\beta > 0.1$. The *MAD-X* not linear model is no more approximated by first order analysis.

5.5.2 Accuracy limits MKP kickers

In order to study limits for this algorithm we took into analysis one single kick trying to reconstruct with the response matrix defined in the previous section, using 208 lenses . We choose, as a starting point, the case of MKPs reconstruction since they are very close each other. MKPA.11931, MKPA.11936, MKPC.11952, MKP.11955 are injection kickers placed from 615m to 624m in SPS (compare in Figure 5.4). The phase length for the FODO cell that contains MKPs is almost 180°. We will study reconstruction in the vertical plane. Looking to Table B.1 in Appendix B we see that the corresponding beta function in the vertical plane decreases from 96.6m to 59.6m.

Before starting simulations, we can compute the quadrupolar error ΔK expected value, inverting formula (4.1) obtaining:

$$\frac{\Delta K}{\Delta N_b} = \frac{e^2 c}{2\sqrt{\pi}\sigma_z E} Im(Z_\perp)_{eff} \tag{5.3}$$

where we assumed the smooth approximation relation $< \beta_{av} > \simeq R/Q_y$ with R the machine radius (for example in SPS we have $< \beta_{av} > \simeq 1100/26.18 = 41.9$ m for the vertical plane).MKP kickers in SPS, have $Im(Z_\perp)_{eff}$ in the range $0.2M\Omega, 1M\Omega$ (Tables can be found in [18]). If we take only one kicker, MKP.11936 for example, using equation (5.3) the equivalent quadrupolar error is in the order of $7{\cdot}10^{-6}, 3{\cdot}10^{-5}$, i.e. in the '1' section in Figure 5.11. We expect to find limitations from measured

phase accuracy in SUSSIX, and this is what happens looking to Figure 5.12. Wrong sampling provokes an oscillations in phase advance detection.

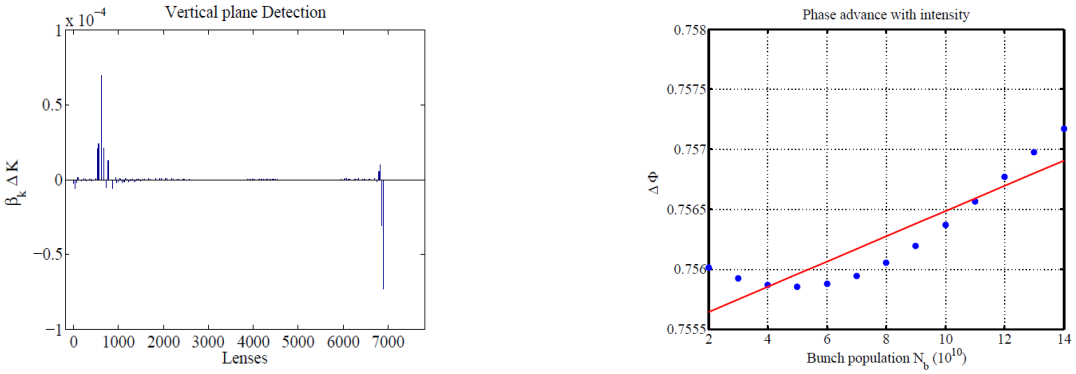

Figure 5.12: Single MKP reconstruction. ΔK refers to thin lens error slope with intensity. The phase advance is presents sinusoidal oscillations since we work below *SUSSIX* accuracy.

If we take all four MKPs, we expect to have 4 times their strength, and then be able to detect an impedance with $Im(Z_\perp)_{eff}$ in the range $0.8M\Omega, 4M\Omega$, corresponding to ΔK_{eq} in the range of $3 \cdot 10^{-5}, 10^{-4}$, i.e. in the '2' section in Figure 5.11. In Figure 5.13 we show the reconstruction using all MKPs. The result, also in phase advance measurement is better than the previous one.

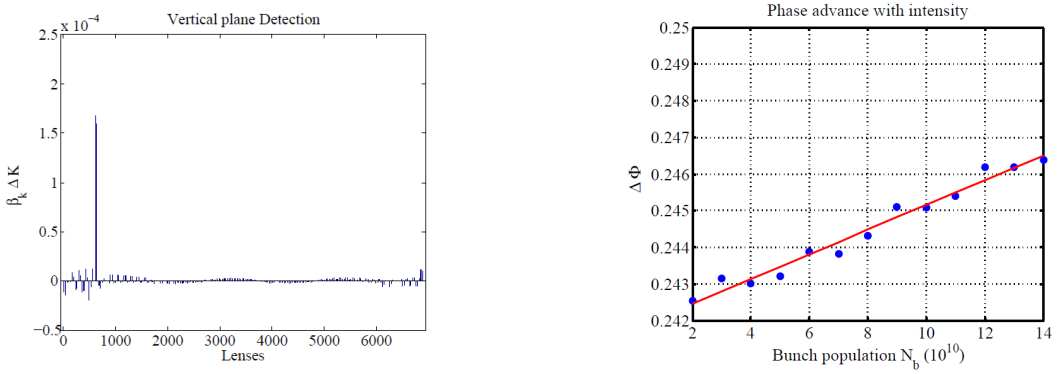

Figure 5.13: All MKPs reconstruction. ΔK refers to thin lens error slope with intensity. The phase advance is well detected since we work above *SUSSIX* accuracy.

In order to study also the '3' section in Figure 5.11, where instabilities from non linear behaviour starts to rise, we artificially increased by a factor 100 the wakes for MKPA.11936 and tried the reconstruction. The result is reported in Figure 5.14. Choosing a short range of intensities $(10^{10} - 4 \cdot 10^{10})$ the reconstruction works as in the previous case, but increasing to $9 \cdot 10^{10}$ we start to have instable behavior. Particular attention, then, has to be kept in these cases.

This analysis sets the range of detectable impedances between $2M\Omega/m$ and $20M\Omega/m$. Since the highest single source of impedance is around $200k\Omega/m$, and

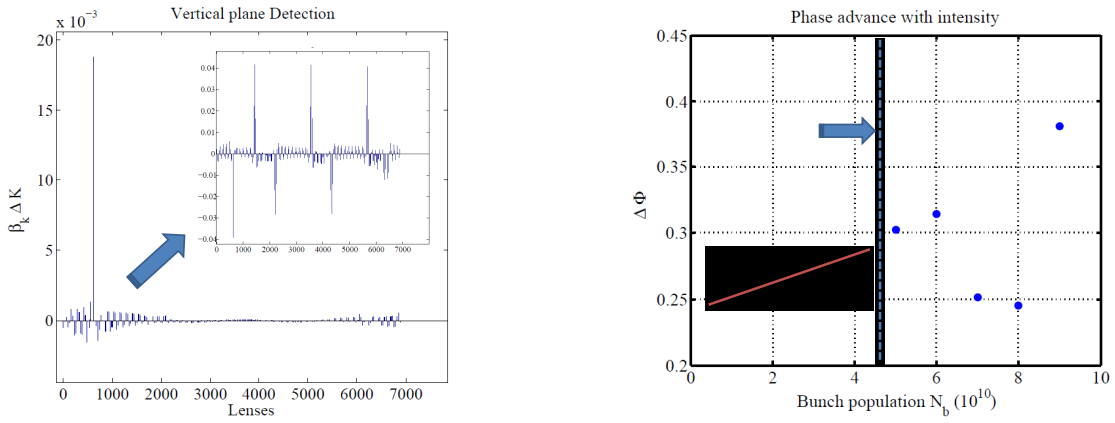

Figure 5.14: Single MKPx100 reconstruction. ΔK refers to thin lens error slope with intensity. Problems in tune shift, beam stability, and reconstruction, can arise.

the whole SPS impedance is in the order of $20M\Omega/m$, these are particularly high values that could explain our previous bad reconstruction in term of accuracy limit in phase detection.

Chapter 6

Conclusions

In this thesis work, we used HEADTAIL macroparticle simulations to analyze the algorithm used to detect sources of transverse impedances in the SPS. In order to test the algorithm we performed a series of simulations that focused our attention on the response matrix used to reconstruct the phase advance beating signal. This matrix is determined by the scheme of lenses used for reconstructing, that is conditioned by the SPS lattice. Moreover some limitations are directly correlated with the linearity assumptions behind the algorithm. In the following we summarize a series of possible further upgrades:

1 The response matrix is computed either with formulae or *MAD-X* and can be used also for reconstruction in the hypothesis of $10^{-4} < \Delta K_{eq} < 10^{-3}$. Future plans include to apply directly the non linear model in reconstruction, or linearizing the response matrix in order to work in a desired range of impedances (analogous to a first order Taylor expansion).

2 The lower limit in reconstruction is determined by the phase accuracy in *SUSSIX*. Since the phase accuracy law is given by [38], [39]:

$$\sigma_\phi \propto \frac{1}{SNR\sqrt{N-1}} \tag{6.1}$$

where σ_ϕ is the phase accuracy in a sampled signal, N is the number of samples (i.e. the number of turns in *HEADTAIL*), SNR is the signal-noise power ratio.

In order to increase the lower bound is possible to increase the number of turns or the SNR. The first one can be easily done, but only in simulation, since in SPS, 512 is the usual number of turns one can reach, the second one can be obtained increasing the displacement of the beam at injection or moving the betatron tune close to half resonance. In this way, the beam will execute larger betatron oscillations increasing the signal power. In our simulation we displaced the beam for 1mm, the maximum achievable is 1cm.

Future plans include also implementing a Fourier Analysis on the complex signal (x, p_x), where x is the bunch centroid position and p_x its momentum, in order to increase our accuracy. This could be possible using BPMs able to measure bunch position in both planes [40].

3 In order to increase the equivalent strength $\beta_k \Delta K / \Delta N_b$, one could try to implement *beta bumps* in the accelerator. A beta bump is a localized increased

value of beta function one can obtain using a set of 4 or more independent quadrupoles. Since in SPS we have only two families of quadrupoles, focusing and defocusing, this solution cannot be implemented. However this method could be applied in LHC.

4 To increase the equivalent strength $\beta_k \Delta K$ one could also try to increase directly the impedance with a known factor. This can be done with collimators in which it is possible to change the aperture in order to increase or decrease the impedance.

5 The set of lenses is the primary choice in impedance detection since it will determine the position in which the pseudo-inversion will try to reconstruct the phase advance beating pattern. Fully understanding and optimizing lenses position will be part of a future work. Recursive detections with sliding lenses could also be implemented.

Bibliography

[1] CERN official web site: www.cern.ch.

[2] *"LHC: the guide"* on CERN official web site.

[3] *"LHC Upgrade Scenarios"*, Koutchouk, Jean-Pierre (CERN) ; Zimmermann, Frank (CERN) Imprint 29 Jul 2009. - 6 p. Presented at Particle Accelerator Conference 2009, Vancouver, Canada, 04 - 08 May 2009

[4] *"LHC beam parameters and IR upgrade options "*,Ruggiero, F; Scandale, Walter ; Zimmermann, Frank (CERN), 2nd CARE-HHH-APD Workshop on Scenarios for the LHC Luminosity Upgrade - LHC-LUMI-05 31 Aug - 3 Sep 2005 - Arcidosso, Italy

[5] *"Effects of Direct Space Charge on the Transverse Mode Coupling Instability"*, D.Quatraro, G.Rumolo.

[6] *"Lezioni del corso di Fisica Moderna"* L.Palumbo, M.Migliorati, Aggiornamento A/A 2008-2009.

[7] *"Accelerator Physics"*, S.Y.Lee, 2^{nd} edition.

[8] *"Space Charge Effects and Instabilities"*,L.Palumbo, M.Migliorati (Sapienza, Universita' di Roma and *LNF-INFN*), JUAS 22 January 2010.

[9] *"Single-beam collective phenomena : transverse II Bunched beams"*, F.Sacherer, F.James, 1st International School of Particle Accelerators "Ettore Majorana", Erice, Italy, 10 - 22 Nov 1976, pp.198-218.

[10] *"Linear imperfections"*, O.Brning (CERN), CAS, CERN Accelerator School: Intermediate Course on Accelerator Physics, Zeuthen, Germany, 15 - 26 Sep 2003, pp.129-182

[11] *"Coherent Beam Oscillations and Transverse Impedance in the SPS"*, H.Burkhardt, G.Rumolo,F.Zimmermann, 19 Jun 2002, 8th European Particle Accelerator Conference, Paris, France, 3 - 7 Jun 2002, pp.1449.

[12] *"Introduction to impedance for short relativistic bunches"*, P.L.Morton, SLAC-PUB-6052 February 1993 (A).

[13] *"USPAS course on collective effects"*, E.Metral, G.Rumolo, US Paricle Accelerator School, June 2009. http://uspas.fnal.gov/materials/09UNM/CollectiveEffects.html.

[14] *"Physics of Collective Beam Instabilities in High Energy Accelerators"*, A.W.Chao, John Wiley Sons, 1993

[15] *"Impedance of an infinitely long and axisymmetric multilayer beam pipe: matrix formalism and multimode analysis "*, N.Mounet,Lausanne/CERN,

Geneva, Switzerland, E.Metral, CERN, Geneva, Switzerland, Proceedings of IPAC'10, Kyoto, Japan.

[16] *"Some Simplified Models of Ferrite Kicker Magnet for Calculation of Longitudinal Coupling Impedance"*, H.Tsutsui, 28 Jan 2000.

[17] *'Field Analysis Of A Dielectric-loaded rectangular Waveguide accelerating Structure"*,Liling Xiao, Wei Gai and Xiang Sun, Argonne Natiola Laboratory, Argonne, IL 60439, USA, Proceedings PAC 2001, Chigaco.

[18] *"Impedance model of the CERN SPS and aspects of LHC single-bunch stability"*Salvant, Benoit (CERN), PhD Thesis, Lausanne, EPFL, 04 Mar 2010

[19] *"Quadrupolar transverse Impedance of Simple Models of Kickers "*, B.Salvant, N.Mounet, C.Zannini EPFL, Lausanne/CERN, Geneva, Switzerland, E.Metral, G.Rumolo CERN, Geneva, Switzerland, Proceedings of IPAC'10, Kyoto, Japan.

[20] *"Generalized form factors for the beam coupling impedance in a flat chamber"* N. Mounet (EPFL, Lausanne and CERN, Geneva) and E. Metral (CERN, Geneva)

[21] *"CERN SPS Impedance in 2007"*, E.Mtral, G.Arduini, H.Burkhardt, R.Calaga, F.Caspers, G.Rumolo, B.Salvant, E.Shaposhnikova, B.Spataro, et al. 11th European Particle Accelerator Conference, Genoa, Italy, 23 - 27 Jun 2008, pp.TUPP066.

[22] *"SPS transverse impedance and TMCI"*, B.Salvant et al. APC meeting held on 24/08/2008, web site https://ab-div.web.cern.ch/ab-div/meetings/apc/welcome.html .

[23] *Measurement and Correction of Accelerator Optics*, F. Zimmermann, SLAC PUB 7844 June 1998, Stanford Linear Accelerator Center, Stanford University, Stanford, CA 94309, USA.

[24] Wikipedia: `http://en.wikipedia.org`

[25] *"REGULARIZATION TOOLS: A Matlab package for analysis and solution of discrete ill-posed problems"* P.C.Hansen. Useful tools for general inversion and regularization inversion problems.

[26] *Pratical user guide for HEADTAIL.*, G.Rumolo, F.Zimmermann, SL-Note-2002-036-AP, 2002.

[27] *"Electron cloud simulations: beam instabilities and wakefields"*, G.Rumolo, F.Zimmermann,12 Dec. 2002

[28] *"Recent Developements for the HEADTAIL code: updating and benchmarks"*, D.Quatraro, G.Rumolo, B.Salvant, CERN-ATS-2009-042

[29] *"HEADTAIL upgrade: new features options"*, D.Quatraro, G.Rumolo, B.Salvant, R.Tomas, W.Metral. 18 July 2008

[30] *"MAD-X User Guide"*, web site http://mad.web.cern.ch/mad.

[31] *"SUSSIX: A Computer Code for frequency analysis of non-linear Betatron Motion"*, CERN SL-Note-98-017 (AP)

[32] *"Drive: A Tool to measure Resonance Driving Terms"*, R.Tomas, CERN-AB Division, June 12, 2003.

[33] *"Measurements of Impedance Distributions and instability thresholds in LEP"*, D.Brandt, P.Castro, K.Cornelis, A.Hofmann, G.Morpurgo, G.L.Sabbi, J.Wenninger and B.Zotter, CERN.

[34] *"Localizing Impedance Sources from Betatron Phase Beating in the Cern SPS"*,G.Arduini, C.Carli, F.Zimmermann, CERN, Geneva, Switzerland.

[35] *"Transverse Impedance Localization Using Dependent Optics"*,G.Arduini, R.Calaga, E.Metral, G.Papotti, D.Quatraro, G.Rumolo, B.Salvant, R.Tomas, BNL, Upton, NY; CERN, Geneva, Switzerland.

[36] *"Impedance Localization: HDTL Studies"*, R. Calaga, D. Quatraro, G. Rumolo, R. Tomas. Imp. Meeting, May 30, 2008

[37] *"Introduction to Particle accelerators"*, P.Bryant, JUAS 2010.

[38] *"An Introduction to the Theory of Random Signals and Noise"*,W.B.Davenport (McGraw-Hill, NY,1958).

[39] *"Methods of solving noise problems"*,W.R.Bennett, Proc. IRE 44, 609-638, (1956)

[40] Private communication, R.Tomas, B.Salvant.

Appendix A

HEADTAIL parameters

The following list is the complete set of parameters used during our simulation and for the SC calculation in Chapter 3.

```
Flag_for_bunch_particles_(1->protons_2->positrons_3&4->ions):    1
Switch_for_lattice_model_(0->simplified_1->from_MAD):            1
Average_electron_cloud_density_along_the_ring_(1/m^3):           1.e10
Fraction_of_the_ring_with_electron_cloud:                        0.7
Number_of_macroelectrons:                                        1
Number_of_particles_per_bunch:                                   1.3e10
Horizontal_beta_function_at_the_kick_sections_[m]:               40.
Vertical_beta_function_at_the_kick_sections_[m]:                 40.
Bunch_length_(rms_value)_[m]:                                 0.149705
Normalized_horizontal_emittance_(rms_value)_[um]:                3.0
Normalized_vertical_emittance_(rms_value)_[um]:                  3.0
Longitudinal_momentum_spread:                              0.000919972
Synchrotron_tune:                                          0.00418669
Momentum_compaction_factor:                                      0.00192
Ring_circumference_length_[m]:                                   6911.5038
Relativistic_gamma:                                              27.7286
Number_of_laps:                                                  512
Multiplication_factor_for_pipe_axes                              10
Multiplication_factor_for_pipe_axes                              10
Longitud_extension_of_the_bunch_(+/-N*sigma_z)                    2
Horizontal_tune:                                                 26.13
Vertical_tune:                                                   26.18
Horizontal_chromaticity_[Q'x]:                                   0.0
Vertical_chromaticity_[Q'y]:                                     0.0
Flag_for_synchrotron_motion:                                     1
Scale_factor_for_electrons_size:                                 4
Switch_for_wake_fields:                                          1
Switch_for_pipe_geometry_(0->round_1->flat):                     9
Res_frequency_of_broad_band_resonator_[GHz]:                     1.3
Transverse_quality_factor:                                       1.
Transverse_shunt_impedance_[MOhm/m]:                             0.0
```

```
Res_frequency_of_longitudinal_resonator_[MHz]:                    200
Longitudinal_quality_factor:                                      140.
Longitudinal_shunt_impedance_[MOhm]:                              0.0
Flag_for_the_tune_spread_(0->no_1->space_charge_2->random):       0
Flag_for_the_e-field_calc_method_(0->no_1->soft_Gauss_2->PIC):    0
Magnetic_field_(0->no_1->dipole_2->solenoid_3->combined):         0
x-kick_amplitude_at_t=0_[m]:                                      0.001
y-kick_amplitude_at_t=0_[m]:                                      0.001
Flag_for_the_proton_space_charge:                                 0
Solenoid_field_[T]:                                               0.004
Switch_for_amplitude_detuning:                                    0
El_distrib_(1->Rect_2->Ellip_3->[1_strp]_4->[2_strp]_5->Parab):   1 1
Linear_coupling_switch(1->on_0->off):                             0
Linear_coupling_coefficient_[1/m]:                                0.0015
Average_dispersion_function_in_the_ring_[m]:                      0.
Position_of_the_stripes_[units_of_sigmax]:                        3.0
Width_of_the_stripes_[units_of_sigmax]:                           0.5
Kick_in_the_longitudinal_direction_[m]:                           0.
Number_of_turns_between_two_bunch_shape_acquisitions:             1000
Switch_for_multiple_bpm_acquisition_(1->on):                      1
Main_rf_voltage_[V]:                                              3.e+6
Main_rf_harmonic_number:                                          4620
Initial_2nd_rf_voltage_[V]:                                       0.
Final_2nd_rf_cavity_voltage_[V]:                                  0.7e+6
Harmonic_number_of_2nd_rf:                                        18480
Relative_phase_between_cavities:                                  3.1415
Start_turn_for_2nd_rf_ramp:                                       25000
End_turn_for_2nd_rf_ramp:                                         26000
Sextupolar_kick_switch(1->on_0->off):                             0
Sextupole_strength_[1/m^2]:                                       -0.254564
Dispersion_at_the_sextupoles_[m]:                                 2.24
Switch_for_losses_(0->no_losses_1->losses):                       0
Second_order_horizontal_chromaticity_(Qx''):                      0.
Second_order_vertical_chromaticity_(Qy''):                        0.
Switch_for_boundary_conditions(0->open_space_1->rect_box):        0
Conductivity_of_the_resistive_wall_[1/Ohm/m]:                     1.e6
Length_of_the_resistive_wall_[m]:                                 0.
Switch_for_beta:                                                  0
Switch_for_wake_table:                                            0
Linear_Rate_of_Change_of_Momentum_[GeV/c/sec]:                    46.
Second_Order_Momentum_Compaction_Factor:                          0.1
```

Appendix B

Wakes for SPS kickers

B.1 Kicker twiss functions

NAME	S	MUX	BETX	MUY	BETY
"MKQH.11653"	524.6862	1.959533543	64.51628235	1.986110525	34.65209017
"MKQV.11679"	535.7712	1.997630621	33.88205233	2.024249238	62.94758529
"MKDV.11731"	550.619	2.095854018	25.67947289	2.053248547	78.25302351
"MKDV.11736"	553.81	2.113831788	31.20930219	2.060275424	66.79596733
"MKDH.11751"	556.021	2.124369916	35.78009155	2.06585583	59.55439591
"MKDH.11754"	557.92	2.132343484	40.18895797	2.071196781	53.7900798
"MKDH.11757"	559.819	2.139449341	45.04422626	2.077118704	48.44657303
"MKPA.11931"	615.0954	2.33941158	26.32846668	2.298979252	96.60298856
"MKPA.11936"	618.7174	2.359067789	32.83381198	2.305506872	80.7756442
"MKPC.11952"	620.6964	2.368100716	37.06977088	2.309613218	72.85119643
"MKP.11955"	624.3184	2.382067863	46.06987592	2.318360739	59.67161827
"MKE.41631"	3973.3482	15.00991737	91.97415894	15.0428801	21.37674886
"MKE.41634"	3975.6612	15.01414839	82.3263877	15.05901934	24.42151839
"MKE.41637"	3977.9742	15.01888679	73.33602927	15.07308061	28.13844096
"MKE.41651"	3980.2872	15.02421954	65.00308367	15.08526053	32.52751658
"MKE.41654"	3982.6002	15.0302514	57.32755088	15.09579611	37.58874525
"MKE.61631"	6277.1828	23.72035683	92.08511936	23.77825569	26.83782874
"MKE.61634"	6279.4958	23.72458282	82.42272868	23.79101399	31.08775627
"MKE.61637"	6281.8088	23.72931579	73.41858917	23.80202355	36.0209479

Table B.1: Kicker Twiss table

B.2 Kicker wake fields

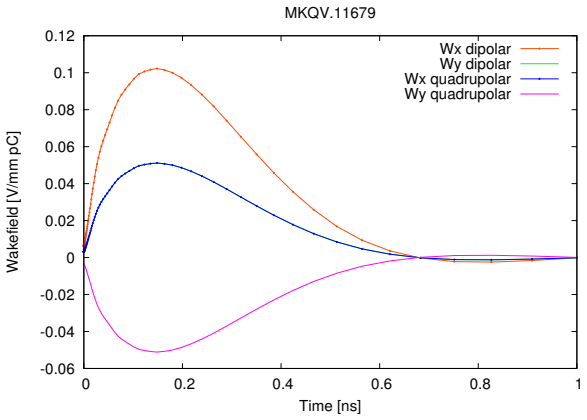

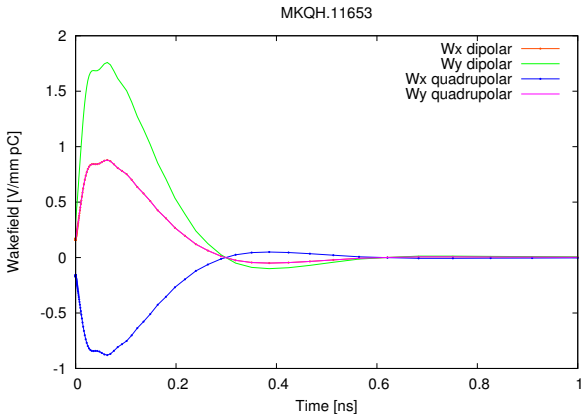

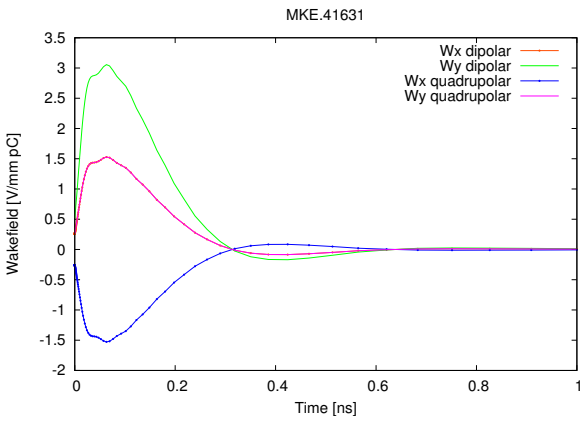

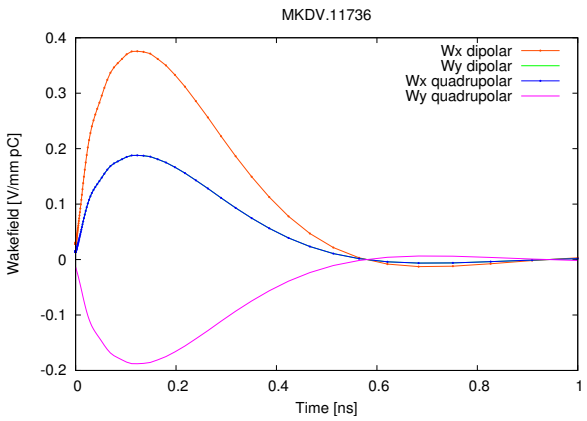

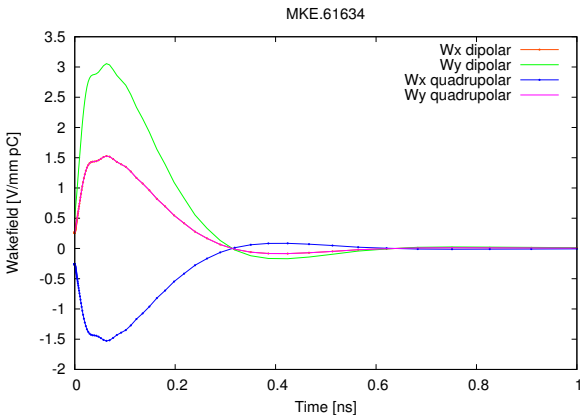

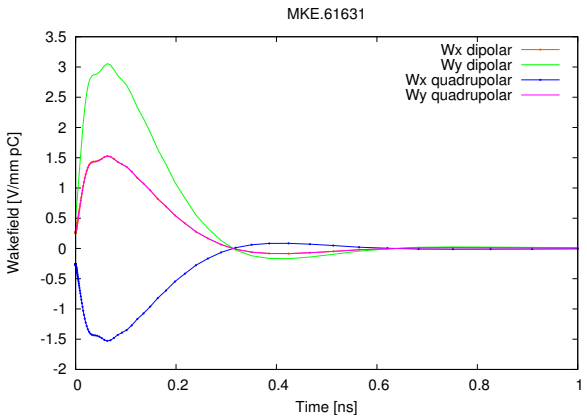

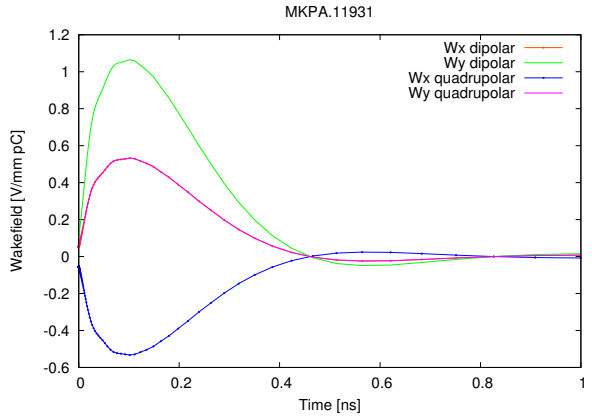
MKPA.11931
Wx dipolar
Wy dipolar
Wx quadrupolar
Wy quadrupolar
Wakefield [V/mm pC]
Time [ns]

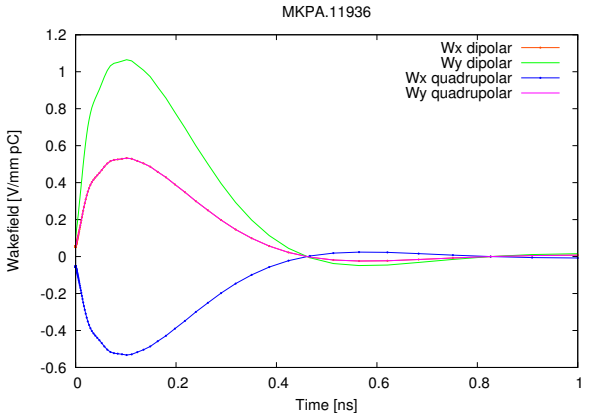
MKPA.11936
Wx dipolar
Wy dipolar
Wx quadrupolar
Wy quadrupolar
Wakefield [V/mm pC]
Time [ns]

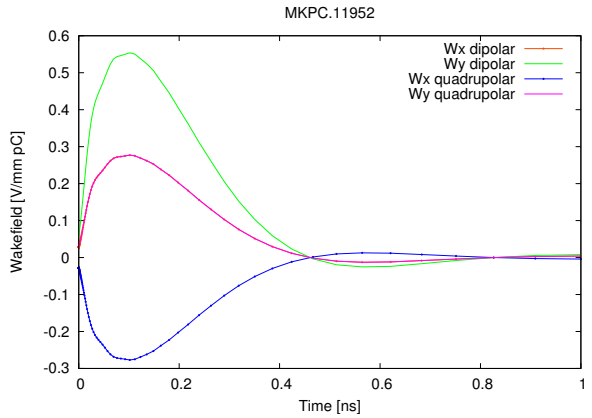
MKPC.11952
Wx dipolar
Wy dipolar
Wx quadrupolar
Wy quadrupolar
Wakefield [V/mm pC]
Time [ns]

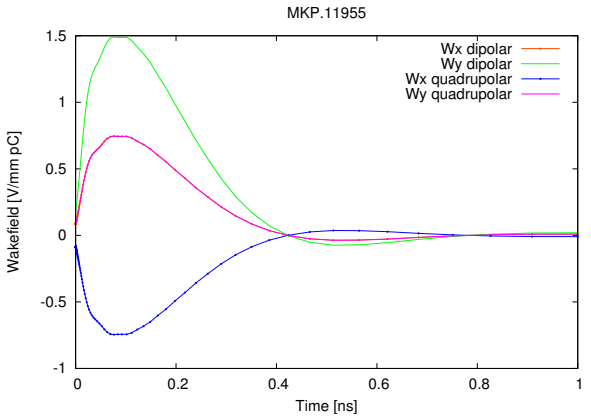
MKP.11955
Wx dipolar
Wy dipolar
Wx quadrupolar
Wy quadrupolar
Wakefield [V/mm pC]
Time [ns]

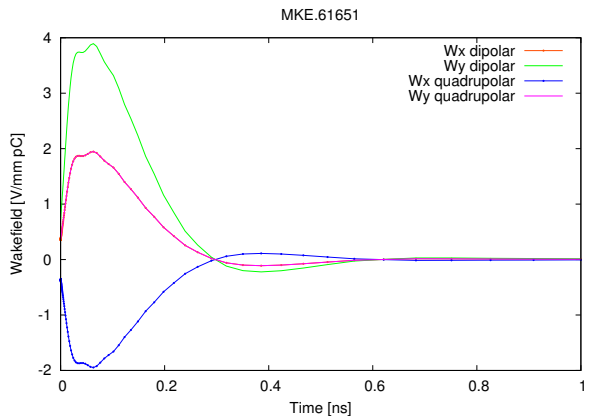
MKE.61651
Wx dipolar
Wy dipolar
Wx quadrupolar
Wy quadrupolar
Wakefield [V/mm pC]
Time [ns]

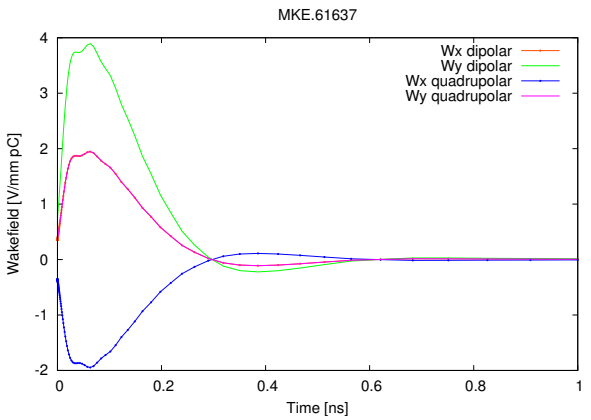
MKE.61637
Wx dipolar
Wy dipolar
Wx quadrupolar
Wy quadrupolar
Wakefield [V/mm pC]
Time [ns]

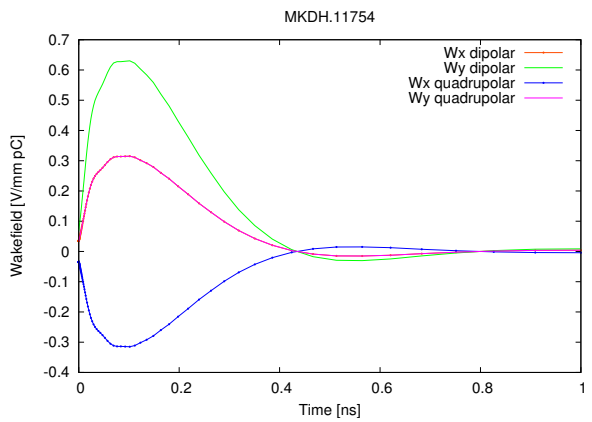
MKDH.11754
Wx dipolar
Wy dipolar
Wx quadrupolar
Wy quadrupolar
Wakefield [V/mm pC]
Time [ns]

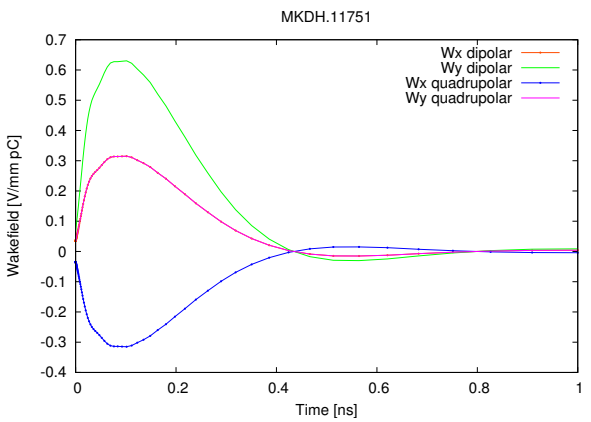
MKDH.11751
Wx dipolar
Wy dipolar
Wx quadrupolar
Wy quadrupolar
Wakefield [V/mm pC]
Time [ns]

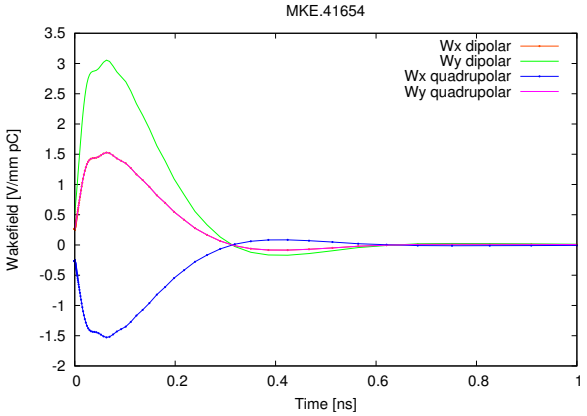
MKE.41654
Wx dipolar
Wy dipolar
Wx quadrupolar
Wy quadrupolar
Wakefield [V/mm pC]
Time [ns]

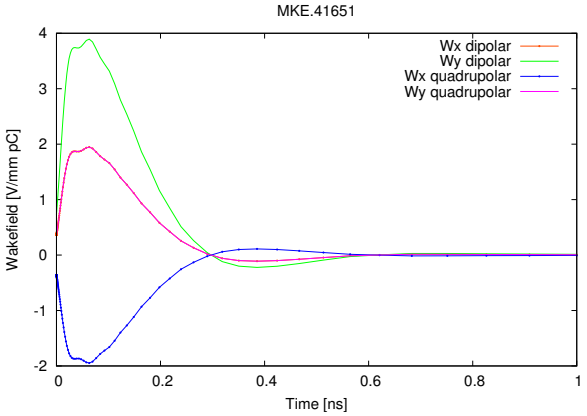
MKE.41651
Wx dipolar
Wy dipolar
Wx quadrupolar
Wy quadrupolar
Wakefield [V/mm pC]
Time [ns]

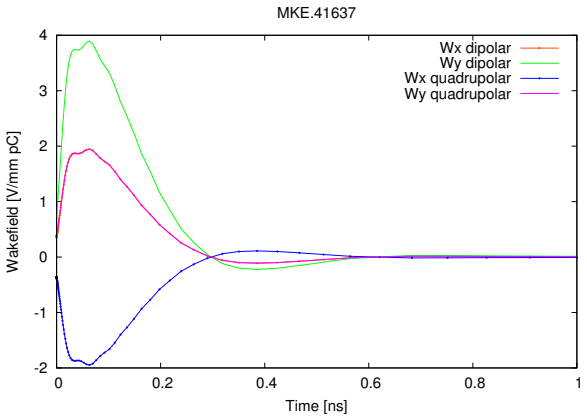
MKE.41637
Wx dipolar
Wy dipolar
Wx quadrupolar
Wy quadrupolar
Wakefield [V/mm pC]
Time [ns]

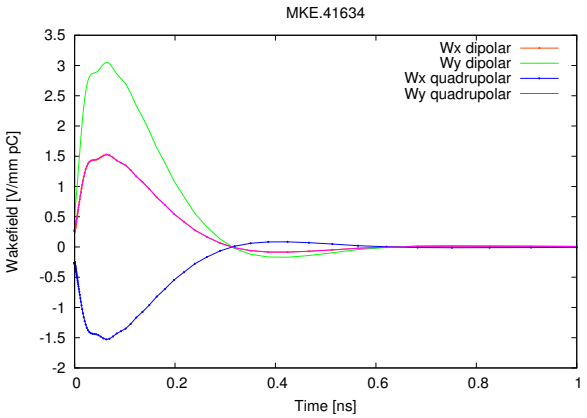
MKE.41634
Wx dipolar
Wy dipolar
Wx quadrupolar
Wy quadrupolar
Wakefield [V/mm pC]
Time [ns]

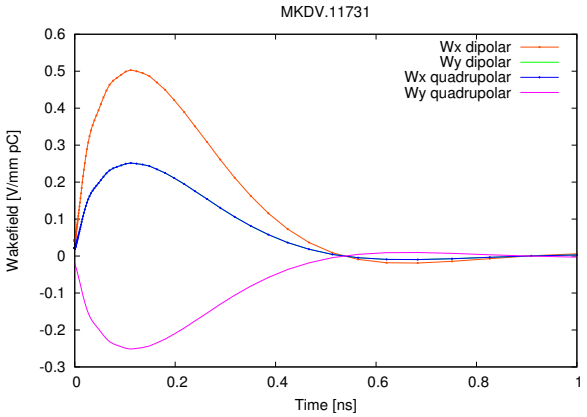
MKDV.11731
Wx dipolar
Wy dipolar
Wx quadrupolar
Wy quadrupolar
Wakefield [V/mm pC]
Time [ns]

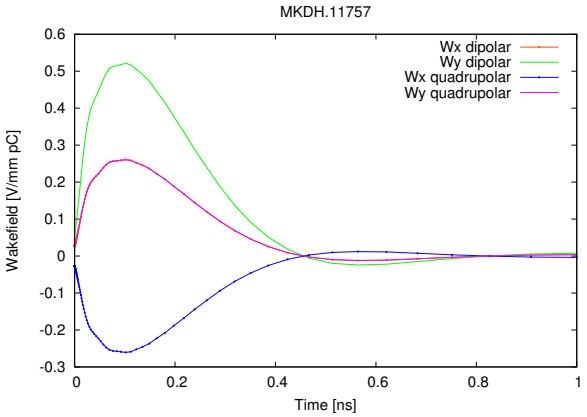
MKDH.11757
Wx dipolar
Wy dipolar
Wx quadrupolar
Wy quadrupolar
Wakefield [V/mm pC]
Time [ns]

Ringraziamenti

Sono molte le persone che hanno contribuito a dar forma a questo lavoro e sarà difficile, per dirla nel gergo di questa tesi, "localizzarle" tutte: dietro ogni riga ci sono giorni e notti di lavoro, ore di discussioni con i miei colleghi e Benoit, momenti di felicità e di stanchezza.

Ringrazio innanzitutto i proff. L.Palumbo ed E.Iarocci che hanno reso possibile fin dall' inizio la realizzazione di quest' esperienza al CERN, credendo fermamente nelle mie capacità e dandomi la preziosa opportunità di crescere sia nel lato professionale che umano.

Ringrazio M.Migliorati per la sua costante presenza, nel momento di avvio del mio lavoro a Roma, e in seguito nonostante la distanza: insieme a Benoit è stato un importante punto di appoggio e concretizzazione.

Non ci saranno mai abbastanza parole per ringraziare Benoit, per avermi seguito da vicino e aver condiviso con me ogni momento nel mio lavoro, dalla teoria dei wake, alla pratica dell'implementazione dell'algoritmo di localizzazione, e infine per aver condiviso con me il momento più importante: la discussione a Roma. Grazie a lui non ho avuto alcuna difficoltà ad inserirmi al CERN ed in particolare nell' ICE section. Persone come G.Arduini, E.Di Benedetto, R.Calaga, E.Métral, N.Mounet, D.Quatraro, G.Rumolo, G.Sterbini, R.Tomàs, C.Zannini, sono state di estremo aiuto dimostrando sempre una completa disponibilità, grande competenza e apertura verso il mio lavoro, condividendo liberamente le loro esperienze, osservazioni e conoscenze.

Molto importante per me stato anche il sostegno dei miei amici a Roma, in particolare Emanuele e Paul che hanno osservato e condiviso più da vicino questa mia esperienza. Un ringraziamento particolare va a Cedric, per la sua amicizia, il buonumore, e la passione che abbiamo condiviso nel nostro quotidiano appuntamento alle 8.30 in caffetteria.

Infine, ma non meno importante, c'è la mia famiglia, mio padre, mia madre, Susanna, che da Roma, e a Ginevra, mi hanno sostenuto nei momenti di maggiore stress e stanchezza, e Alice, che mi ha dato l'energia necessaria a superare lunghe notti lavorative.

L'ultimo ringraziamento è per Colui che costantemente mi ha assistito e guidato in questi mesi di forte passaggio e di nuove avventure.